UNIVERSIDADE
BEIRA INTERIOR

Numerical Analysis of a Centrifugal Pump in OpenFOAM

Pedro Miguel da Silva Gouveia

Dissertação para obtenção do Grau de Mestre em
Engenharia Aeronáutica
(Ciclo de estudos integrado)

Orientador: Prof. Doutor André Resende Rodrigues da Silva
Co-orientador: Prof. Doutor Leandro Barbosa Magalhães
Co-orientador: Eng. Horácio Moreira

Outubro de 2024

Declaração de integridade

Eu, Pedro Miguel da Silva Gouveia, que abaixo assino, estudante com o número de inscrição a41241 de/o Mestrado Integrado em Engenharia Aeronáutica da Faculdade de Engenharia, declaro ter desenvolvido o presente trabalho e elaborado o presente texto em total consonância com o **Código de Integridades da Universidade da Beira Interior**.

Mais concretamente afirmo não ter incorrido em qualquer das variedades de Fraude Académica, e que aqui declaro conhecer, que em particular atendi à exigida referenciação de frases, extratos, imagens e outras formas de trabalho intelectual, e assumindo assim na íntegra as responsabilidades da autoria.

Universidade da Beira Interior, Covilhã 04/10/2024

Assinado por: **Pedro Miguel da Silva Gouveia**
Num. de Identificação: 14668951
Data: 2024.10.04 11:24:50+01'00'

Dedicatória

Aos meus pais, ao meu irmão e à Adriana.

Agradecimentos

Esta dissertação tem seguimento do projeto BoCAGE (Bombas Criogénicas para Aplicação Geoespacial) gerido pela Omnidea, Lda, cujo objetivo fora a construção de uma bomba centrífuga criogénica para um veículo sub-orbital. Desta forma, o meu primeiro agradecimento é direcionado para toda a empresa, principalmente para o meu co-orientador Engenheiro Bruno Porto. Não poderia também esquecer mencionar o Engenheiro João Vale que dedicou parte do seu tempo para minha mentoria.

Em segundo lugar, gostaria de agradecer não apenas ao meu Orientador Professor Doutor André Silva, que se mostrou disponível para me alocar qualquer recurso necessário para o melhor desempenho na minha dissertação, como também ao meu co-orientador académico, Professor Doutor Leandro Barbosa Magalhães. Foi ele que realmente me introduziu ao mundo da Dinâmica de Fluidos Computacional (DFC) e me alertou para a extrema importância dos primeiros passos em DFC antes de passar para as ditas simulações.

Gostaria também de mencionar os meus colegas universitários e amigos pessoais por me ensinarem a crescer como pessoa dentro de uma comunidade forte e unida. Ao Hugo e ao Sérgio quero deixar uma palavra forte de agradecimento pelas memórias criadas durante estes seis anos. Memórias principalmente de riso e alegria, mas também de momentos de incerteza acerca do nosso desempenho académico. À minha melhor amiga e namorada Adriana. É graças a ela que sou uma pessoa mais paciente e altruísta. Quero-te agradecer por teres sido quem mais me apoiou nos piores momentos da minha vida pessoal, e esteve comigo para criar memórias que permanecerão para o resto das nossas vidas. Espero continuar a crescer convosco nesta nova etapa que se segue, nunca deixando de relembrar como nos conhecemos e aquilo que ainda temos para viver.

Finalmente, agradecer à minha família pela educação que me deram. Independentemente da possibilidade de reverter várias situações nas nossas vidas, a verdade é que é graças a elas que sou quem sou e estou onde estou. Não mudaria grande coisa destes últimos quase 24 anos. Do fundo do meu coração, Marco, Mãe e Pai. Obrigado.

Resumo

Esta dissertação investiga o desenvolvimento e a validação de um modelo numérico para a análise de bombas centrífugas utilizando o software OpenFOAM v11. O foco principal foi na simulação de bombas operando com fluido de massa volúmica constante e variação mínima de temperatura. O modelo foi validado com dados experimentais da literatura, utilizando as equações de Navier-Stokes com aproximação RANS e o modelo de turbulência $k - \varepsilon$. Os resultados numéricos para parâmetros globais, como a altura manométrica total e a potência, mostraram uma concordância de até 4.30% e 4.37% de erro em relação aos dados experimentais, respetivamente, e o ponto de melhor eficiência foi previsto com um desvio de 3.73%.

Adicionalmente, foi inicialmente prevista a análise do desempenho de uma bomba desenvolvida pela Omnidea, Lda. Contudo, as simulações dessa bomba foram descartadas devido a falta de recursos computacionais e tempo insuficiente para implementar os modelos de cavitação e escoamento bifásico necessários. A ausência desses modelos impossibilitou a representação precisa de zonas onde a pressão cai abaixo da pressão de vapor do fluido, fator crítico em aplicações criogênicas. Assim, concluiu-se que o modelo numérico utilizado é adequado para escoamentos simples, mas requer melhorias para ser aplicado em simulações mais complexas.

Os resultados indicam que, embora o método seja eficiente para a análise de bombas sem cavitação, estudos futuros devem incorporar modelos mais avançados de escoamento bifásico e cavitação para permitir uma análise mais precisa em sistemas de alta performance.

Palavras-chave

Bomba Centrífuga, Motor Foguete, OpenFOAM, Reynolds-averaged Navier-Stokes

Abstract

This dissertation investigates the development and validation of a numerical model for the analysis of centrifugal pumps using the OpenFOAM v11 software. The primary focus was on simulating pumps operating with constant fluid density and minimal temperature variation. The model was validated against experimental data from the literature, using the Navier-Stokes equations with RANS approximation and the $k - \varepsilon$ turbulence model. Numerical results for global parameters, such as total head and power, showed an agreement with errors of 4.30% and 4.37% compared to experimental data, respectively, and the best efficiency point was predicted with a 3.73% deviation.

Additionally, the performance of a pump developed by Omnidea, Lda. was initially intended to be analyzed. However, these simulations were discarded due to lack of computational resources and insufficient time to implement the necessary cavitation and multiphase flow models. The absence of these models made it impossible to accurately represent regions where the pressure drops below the fluid's vapor pressure, a critical factor in cryogenic applications. Therefore, it was concluded that the numerical model used is suitable for simple flow conditions but requires improvements to be applied in more complex simulations.

The results suggest that, while the method is efficient for pump analysis in non-cavitating conditions, future studies should incorporate more advanced cavitation and two-phase flow models to enable more accurate analysis in high-performance systems.

Keywords

Centrifugal Pump, Rocket Engine, OpenFOAM, Reynolds-Averaged Navier-Stokes

Contents

List of Figures

List of Tables

Nomenclature

$\vec{\mathrm{a}}$	General vector property	-
i	Incidence Angle	-
I	Turbulent Intensity	[%]
k	Turbulent kinetic energy	$[\mathrm{m^2\,s^{-2}}]$
l_t	Turbulent length scale	$[\mathrm{m}]$
$\dot{\mathrm{m}}$	Mass Flow Rate	$[\mathrm{kg\,s^{-1}}]$
n	Rotor Speed	$[\mathrm{rad\,s^{-1}}]$
$\mathrm{n_q}$	Specific Speed	$[\mathrm{rad\,m^{3/2}s^{-3/2}}]$
Q	Volumetric Flow Rate	$[\mathrm{m^3\,h^{-1}}]$
p	Static Pressure	[Pa]
$\mathrm{p_h}$	Hydrostatic Pressure	[Pa]
P	Power	[W]
r	Radius	$[\mathrm{m}]$
r	Position	$[\mathrm{m}]$
Re	Reynolds Number	-
T	Temperature	[K]
u	Velocity	$[\mathrm{m\,s^{-1}}]$
u_τ	Friction Velocity	$[\mathrm{m\,s^{-1}}]$
u^+	Dimensionless Velocity	-
v	Peripheral Tangential Velocity	$[\mathrm{m\,s^{-1}}]$
w	Relative Velocity	$[\mathrm{m\,s^{-1}}]$
y	Wall Distance	$[\mathrm{m}]$
y^+	Dimensionless Wall Distance	-
Y	Specific Work	$[\mathrm{m^2\,s^{-2}}]$
α	Angle in the Absolute Reference Frame	[rad]
β	Angle in the Relative Reference Frame	[rad]
δ	Deviation Angle, Boundary layer thickness	[rad], $[\mathrm{m}]$
Γ	Diffusion Coefficient	-
Γ_t	Turbulent Diffusivity	$[\mathrm{kg\,m^{-1}\,s^{-1}}]$
ε	Turbulent Kinetic Energy Dissipation Rate	$[\mathrm{m^2\,s^{-3}}]$
κ	von Kármán Constant	-
μ	Molecular Dynamic Viscosity	$[\mathrm{N\,s\,m^{-2}}]$
μ_t	Turbulent Viscosity	$[\mathrm{N\,s\,m^{-2}}]$
ν	Kinematic viscosity	$[\mathrm{m^2\,s^{-1}}]$
θ	Non-orthogonal angle	[rad]
ρ	Density	$[\mathrm{kg\,m^{-3}}]$

$\overline{\overline{\tau}}$	Shear Stress Tensor	$[\mathrm{N\,m^{-2}}]$
ϕ_f	Dissipation Function	$[\mathrm{Pa\,s^{-1}}]$
Φ	Dissipation Function	$[\mathrm{Pa\,s^{-1}}]$
Ψ	Head Coefficient	-
ω	Angular Velocity, Turbulent Kinetic Energy Specific Dissipation Rate	$[\mathrm{rad\,s^{-1}}]$, $[\mathrm{s^{-1}}]$

Subscripts

0	Quantity measured at design conditions
I	Quantity relative to the inertial frame of reference
opt	Quantity measured at optimal working conditions
R	Quantity relative to the rotating frame of reference
u	Usefull quantity
x	Quantity in the x axis direction
y	Quantity in the y axis direction
z	Quantity in the z axis direction

Superscripts

$+$	Normalized
$\overline{\phi}$	Reynolds Average
$'$	Reynolds Fluctuations

List of Acronyms

2D	Two Dimensional
3D	Three Dimensional
AMI	Arbitrary Mesh Interface
AMR	Adaptive Mesh Refinement
BD	Blending Differencing
CD	Central Differencing
CFD	Computational Fluid Dynamics
CFL	Courant-Friedrichs-Lewy
DNS	Direct Numerical Simulation
FDM	Finite Difference Method
FEM	Finite Element Method
FVM	Finite Volume Method
MRF	Moving Reference Frame
LES	Large Eddy Simulation
NCC	Non Conformal Coupling
NPSH	Net Positive Suction Head
PS	Suction Side of the Blade
RANS	Reynolds-averaged Navier-Stokes
RNG	Re-Normalization Group
SS	Suction Side of the Blade
SST	Shear Stress Transport
UD	Upwind Differencing

Chapter 1

Introduction

Rocket propulsion systems are critical components in the space industry, enabling the delivery of payloads into orbit and beyond. At the heart of these systems lies the challenge of efficiently transporting propellants from storage tanks to the combustion chamber where they are burned to produce thrust. Lighter lower performance rockets do not use centrifugal machines to pump the fuel into the combustion chamber. However, heavier rockets that need to reach higher altitudes need centrifugal pumps to pressurize the propellant. Engines need to achieve very high pressures to create the necessary thrust. Centrifugal pumps are the most effective solution for this task. They typically operate under extreme conditions and meet stringent performance criteria [2].

Centrifugal pumps 2.1.2 in rocket applications are tasked with handling large volumes of liquid propellants, such as liquid hydrogen and liquid oxygen, which are often stored at cryogenic temperatures. These pumps need to operate at high rotational speeds to generate the necessary pressures to move the propellants from low-pressure storage tanks to the high-pressure environment of the combustion chamber. This high-speed operation is essential not only for maintaining the compact size and low mass of the pump but also for achieving the high power-to-weight ratio required in rocketry. However, this comes with significant challenges.

One of the primary difficulties faced by centrifugal pumps in rocket systems is cavitation [4, 6]. Cavitation occurs when the local pressure of the fluid drops below its vapor pressure, leading to the formation of vapor bubbles. As these bubbles move into regions of higher pressure, they collapse violently, potentially causing damage to the pump impeller and other components. In rocket engines, cavitation can lead to a loss of efficiency, increased vibrations, and even catastrophic failure if not properly managed.

The high-speed nature of centrifugal pumps exacerbates the risk of cavitation. As the rotational speed of the pump increases, the pressure on the suction side of the impeller decreases, making it more susceptible to cavitation. This is particularly problematic in the vacuum of space where ambient pressure is extremely low. Designing pumps that can operate at high speeds without cavitation requires careful consideration of fluid dynamics and pump geometry. Advanced techniques, such as the use of inducers—axial flow components placed upstream of the main impeller—help in raising the fluid pressure gradually, thereby mitigating the onset of cavitation. The inducer usually is composed of a set of helical blades that effectively add length that the flow has to traverse before coming into contact with the impeller, which gradually increases fluid pressure, typically around

5-10% of the total pressure rise [2].

Another significant challenge is the mechanical stress imposed on the pump components due to high rotational speeds. The centrifugal forces acting on the pump's impeller and housing can lead to deformation, fatigue, and eventual failure if the materials and design are not optimized for such extreme conditions. The pump must be robust enough to withstand these stresses while maintaining minimal weight to avoid detracting from the overall performance and efficiency of the rocket.

Additionally, the thermal environment in which these pumps operate poses unique challenges. Rocket propellants are often cryogenic, meaning the pump must function effectively at extremely low temperatures. The material properties of the pump components can change drastically at these temperatures, potentially leading to brittleness and reduced performance. Ensuring the pump's reliability under these thermal conditions requires thorough material selection and testing.

In conclusion, centrifugal pumps are indispensable in rocket propulsion systems, but their design and operation involve overcoming significant challenges. High rotational speeds are necessary to minimize the pump's weight and maximize its efficiency, but they increase the risk of cavitation and impose severe mechanical stresses. Addressing these issues through advanced design and analysis, particularly using numerical methods like those provided by OpenFOAM, is crucial for the successful deployment of efficient and reliable rocket propulsion systems.

1.1 Motivation and Objective

This thesis is conducted in collaboration with Omnidea, Lda, which seeks to develop a reliable numerical model for future analysis of rotating machinery. The model will be implemented using open-source software to minimize costs. Throughout the course of this work, Omnidea has been advancing the development of its first centrifugal rocket pump, although experimental data was not available by the conclusion of this thesis.

The primary objective of this dissertation is to provide a thorough analysis of Omnidea's centrifugal pump and compare the results with theoretical predictions generated by in-house scripts. To ensure the accuracy and reliability of the findings, the study will first validate the approach using a lower-speed centrifugal water pump from existing literature as a case study.

1.2 Thesis Outline

The report is made out of five chapters, where the first one introduces the topic and motivation behind the thesis. In Chapter 2 a theoretical background regarding centrifugal pumps alongside a literature review relevant to this topic is presented to the reader. Chapter 3 lays out the fundamental fluid mechanics conservation laws, the approximations needed to perform the numerical calculations and the mathematical models chosen for implementation in OpenFOAM. Chapter 4 covers both domain and equation terms discretization methods and the explanation for their choice. Chapter 5 implements everything that was discussed in the previous chapters. There is a discussion of the obtained results and why they deviate (or not) from experimental/theoretical results. The last Chapter puts forward the recommendations for future work and the conclusions.

Chapter 2

Literature Review and Theoretical Background

2.1 Turbomachinery

2.1.1 What are Turbomachines?

Turbomachines are all the devices in which energy is transferred to or from a continuously flowing fluid by the dynamic action of one or more moving blade rows [3]. However, this general description can illustrate a feed-water pump in a power plant, a wind turbine generating renewable energy, or even a turbopump used to launch satellites to outer space. Turbomachines are grouped into two categories: turbines, where energy is transferred from the fluid into the rotor; pumps/compressors, where energy is transferred into the fluid by an increase in pressure. The term compressor is used for a machine that operates on gases, while pumps operate on liquids. This domain has several sub-categories, but the main focus will be on radial flow turbopumps, with an axial flow pump (also called inducer) mounted upstream. A further categorization of these engineering machines is presented in Figure 2.1.

2.1.2 Centrifugal Pumps

A centrifugal pump is fundamentally composed of a rotating impeller followed by a diffuser. A distinction between the terms ”pump”, ”fan” and ”compressor” must be settled. A ”pump” refers to machines which increase the pressure of a following liquid. A ”fan” imparts only a small pressure increase in pressure to a following gas. The pressure increase is so small that the gas can be considered incompressible. A ”compressor” provides a substantial increase in pressure to a following gas, and compressibility effects are to be taken into consideration [3].

The majority of high speed centrifugal pumps make use of an axial pump upstream of the impeller. This helps in the increase of the NPSH (net positive suction head) when cavitation phenomena is present. A schematic of a typical high speed centrifugal pump is present in Figure 2.2.

Typically, a fluid flowing through an inlet pipe firstly encounters either the inducer (in the case of high-speed centrifugal pumps) or the eye of the inlet or eye of the impeller.

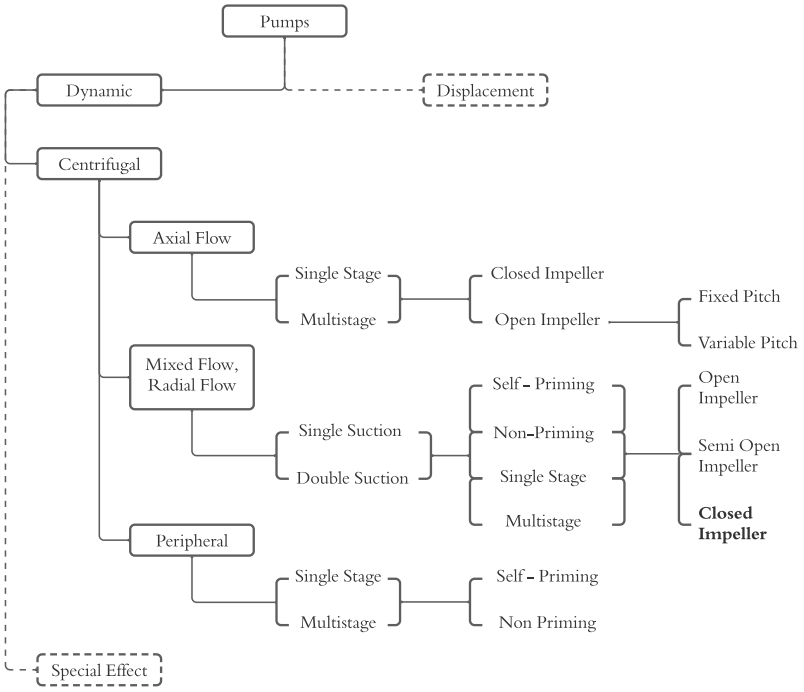

Figure 2.1: Classification of dynamic pumps. Dashed lines mean that the sub levels of those categories are not shown, since there is no interest. Adapted from [4]

The impeller is what increases the energy of the fluid, increasing its pressure and velocity. This fluid then flows into the diffuser, which converts the kinematic energy into pressure energy. This process can be achieved by free diffusion in the annular space surrounding the impeller, or by diffuser vanes which allow a decrease in diffuser size. Outside the diffuser is a volute whose function is to collect the flow and deliver it to the outlet pipe. [3]

2.1.2.1 Flow Physics and Modeling

Radial turbomachines that increase pressure are also known as ”centrifugal” turbomachines due to the influence of the centrifugal effect on the pressure increase. Gases have lower density than liquids and thus, for a given pressure-ratio, experience a higher relative change in density. Liquids can, generally speaking, be considered incompressible. However, in pumps where pressure ratios are experienced, density variations become significant and a compressible analysis is required.

Given the complex 3D motion of the flow inside centrifugal turbomachinery, a complete analysis would require the full set of Navier-Stokes equations to be solved. In order to simplify the motion and obtain a first iteration of the problem, 1D flows can be user, alongside loss models gathered from empirical data. However, the main goal of Omnidea, Lda is to verify the possibility of using OpenFOAM to solve problems containing cryogenics and cavitation.

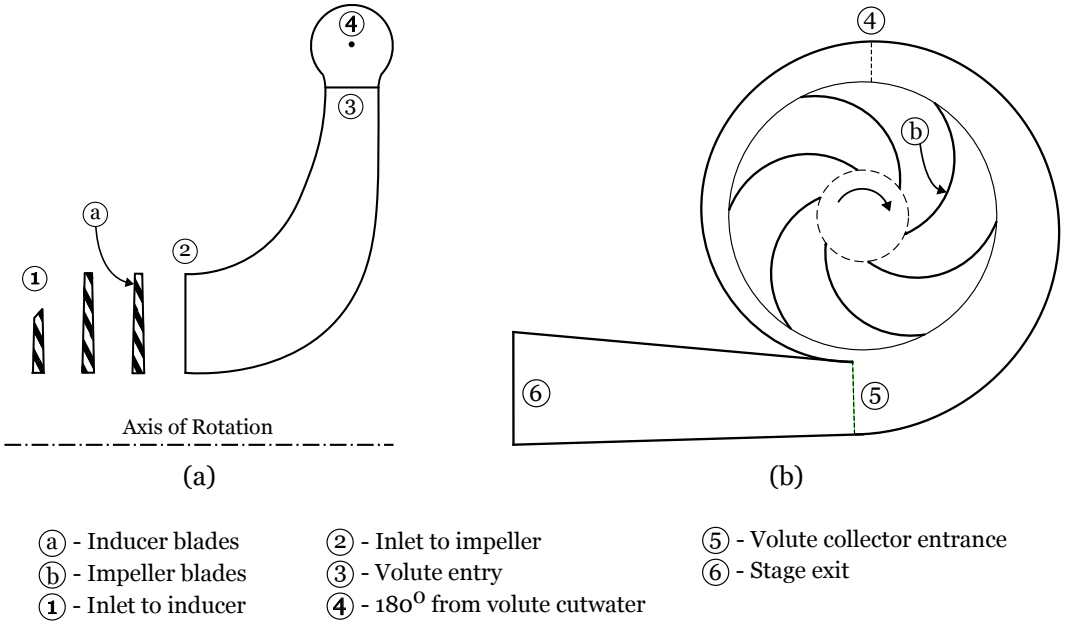

Figure 2.2: (a) Meridional and (b) axial cross sections of one of the several single stages pump layouts utilized in liquid rocket engines.

2.1.3 Performance Data

Centrifugal Pumps are present in a wide range of applications, thus possessing a wide range of characteristics. Nevertheless, any pump application is characterized by its rotor speed, n, volumetric flow rate, $\mathrm{Q_d}$ and head, $\mathrm{H_d}$. These are defined below, according to Gülich [6].

- **Rotor Speed**. It represents the angular velocity at which the pump impeller(s) rotate.

- **Flow Rate**. It is usually defined as the useful volume flow through the discharge nozzle.

- **Specific work / Head and Head Coefficient**. The specific work Y is defined as the total useful energy transmitted by the pump to the fluid per unit of mass. Nevertheless, the head $\mathrm{H} = \mathrm{Y}/\mathrm{g}$ is a parameter preferred by the majority of authors. It is given by Equation (2.1), where subscripts "d" and "s" represent discharge and suction nozzles, respectively. The plane of reference for the z dimension should be chosen at the shaft centerline in the case of horizontal pumps. Meanwhile, the head coefficient is given by Equation (2.2).

$$\mathrm{H} = \frac{\mathrm{p_d} - \mathrm{p_s}}{\rho \mathrm{g}} + \mathrm{z_d} - \mathrm{z_s} + \frac{u_d^2 - u_s^2}{2\mathrm{g}} \quad (2.1)$$

$$\Psi = \frac{2gH}{nD} \quad (2.2)$$

- **Net Positive Suction Head**. This parameter is used when the working liquid's pressure drops below its vapor pressure. This phenomena is known as cavitation. The NPSH is defined as the absolute suction head minus the vapor pressure expressed as head $p_v/(\rho g)$

According to Gülich [6], the performance data of a centrifugal pump is described by the previous three parameters, in addition to the two presented below.

- **Power**. The useful power P_u is obtained by multiplying the transported mass flow (ρQ) by the specific work Y. When simplified, it gives places to the expression presented in Equaion (2.3).

$$P_u = Q\Delta p \quad (2.3)$$

- **Efficiency**. Due to all the losses present in a pump, the required power, P, at the coupling is greater than the useful power, P_u. The ratio between these two parameters is the pump's efficiency, η, given by Equaion (2.4).

$$\eta = \frac{P_u}{P} \quad (2.4)$$

With such a wide range of parameters, it becomes difficult to select a suitable type of impeller for a given application. Consequently, a definition which relates head, rotor speed and volumetric flow rate is widely adopted - the specific speed, n_q, given by Equaion (2.5).

$$n_q = n\frac{\sqrt{Q_{opt}/f_q}}{{H_{opt}}^{0.75}} \quad (2.5)$$

where f_q is the number of impeller entries and the subscript opt denotes quantities measured at optimal conditions. Despite its denomination, the specific speed is not truly a non-dimensional quantity. Even though several definitions of specific speed are available in literature, Equaion (2.5) is the one used throughout it.

2.1.4 Velocity Triangles

In centrifugal pumps design and numerical calculations, two different frames of reference are utilized. A flow described in fixed coordinates is described by an absolute reference

frame, and a relative reference frame described a relative flow. The later one corresponds to a movement that would be seen by an observer rotating with the impeller. The absolute velocity, u, peripheral tangential velocity, v and relative velocity, w, are related by Equation (2.6). When considering a particle adhering to a rotating wall, $w = 0$.

$$u = v + w \quad (2.6)$$

When considering a two dimensional referential, each of these velocity vectors are a sum of two components. It is common practice to make use of cylindrical polar coordinates in centrifugal pumps, instead of the usual Cartesian referential. Consequently, the velocity components will be radial, denoted by the subscript r, and tangential, denoted by the subscript θ. In Figure 2.3 are displayed the velocity triangles in inlet and outlet positions for a centrifugal pump.

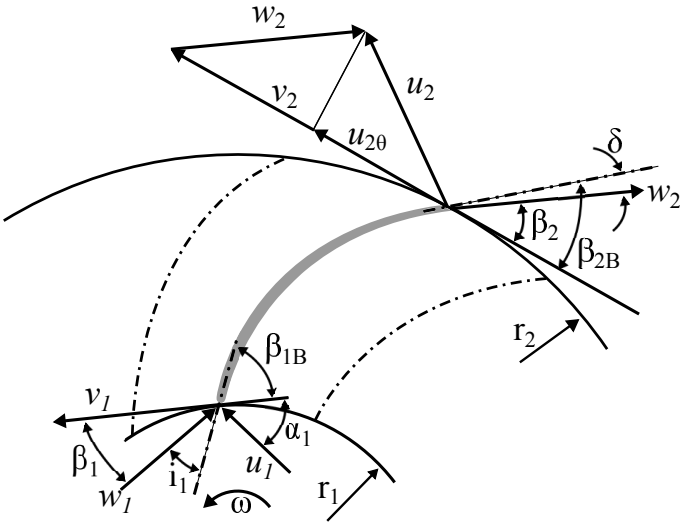

Figure 2.3: Velocity vectors acting on the blade at radial locations equal to impeller inlet and outlet. Adapted from [6]

In Figure 2.3 four relevant angles can be visualized. The incidence angle, i, the angle in the absolute reference frame, α, the angle in the reference frame, β and the deviation angle, δ. The incidence angle represents the difference between the blade angle and the flow angle. Every turbomachinery blade is projected for a certain flow rate. When altering it, the incidence velocity vectors changing, consequently modifying i. If the flow angle and blade angles are identical, $i = 0$, causing a "shockless entry" to happen. On the other hand, if i increases to a certain extent, flow separation might occur. The deviation angle, δ, describes a phenomena of congruent flow over the blade and the idea of deviation of the real flow from the blade outlet angle. [6]. Different sign conventions are utilized for the tangential components of the absolute and relative velocities, u_θ and w_θ, respectively. While the first one is counted as positive when acting in the direction of u, the later one is counted as positive when acting opposite to the direction of u [6].

2.1.5 Centrifugal Pumps for Rocket Engines

The centrifugal pump has played a crucial role in the evolution of pump-fed liquid propellant rocket engines [2]. Its widespread use is attributed to its relative simplicity, reliability, broad operational flow range, and satisfactory performance. Additionally, early rocket programs benefited from the existing expertise in centrifugal pumping systems from the commercial pumping industry.

However, the successful development of centrifugal pumping systems has not been without significant challenges. According to Campbell and Farquhar [7], these challenges are primarily due to the demanding application parameters, such as:

1. A wide variety of design requirements, including flow rate, head rise, and fluid characteristics
2. The importance of very low suction pressure
3. The necessity for high efficiency while achieving a high stage head rise
4. The handling of unknown or difficult-to-manage cryogenic, corrosive, and low-density fluids
5. Very rapid transients during start-up, shutdown, and flow changes

Centrifugal pumps for rocket engines have been developed to handle flow rates ranging from as low as $0.23\ \mathrm{m^3\,h^{-1}}$ to as high as $5700\ \mathrm{m^3\,h^{-1}}$, with most systems operating within the 227 to $2270\ \mathrm{m^3\,h^{-1}}$ range. Pressure requirements for these pumps vary significantly, especially for low-density liquid hydrogen, which demands very large head rises. Rocket engine pumps have been designed for pressure increases from $4.8\ \mathrm{MPa}$ to approximately 34.5-$41.4\ \mathrm{MPa}$, translating to head-rise values of $457\ \mathrm{m}$ to $3658\ \mathrm{m}$ for water-like density fluids, and from $6096\ \mathrm{m}$ to nearly $60\,960\ \mathrm{m}$ for hydrogen. The specific speeds of pumps in operational systems range from 9.7 to 38.8 (in rpm, $\mathrm{m^3\,s^{-1}}$, and m units), with the majority falling between 11.63 and 29. These relatively low values are influenced by the requirements for high head rise, low suction pressure limits, and the mechanical speed limits of the drive system. Rocket pumps generally have low operational durations: pumps used in ballistic missiles typically run for 2 to $5\ \mathrm{min}$, while those in space vehicles operate for 1 to $10\ \mathrm{min}$. Emerging applications, such as nuclear and chemical space shuttles, may demand multiple mission cycles lasting up to $20\ \mathrm{min}$ each, with a total usable life of up to $10\ \mathrm{h}$. The number of operational cycles has varied from a single use to recent requirements of up to 100 cycles. Testing has often involved several multiples of these operating durations, but accruing more than a few hours of operating time on a single unit has been uncommon [7].

2.2 State-Of-The-Art

Throughout the last decades, the employment of Computational Fluid Dynamics in turbomachinery has been extensively implemented, mostly due to the growing availability of computational resources and progress in the accuracy of numerical simulations (Shah et al. [8]). The study of centrifugal pumps, particularly their numerical modeling and performance optimization, has seen significant advancements in recent years. This subsection provides a detailed review of the current state-of-the-art in centrifugal pump research, covering key areas such as computational fluid dynamics (CFD), cavitation modeling, turbulence modeling, and optimization techniques.

2.2.1 Advancements in Computational Fluid Dynamics (CFD)

Recent progress in computational fluid dynamics has significantly enhanced the accuracy and efficiency of centrifugal pump simulations. CFD has become a vital tool for analyzing fluid flow within pumps, enabling detailed visualization and prediction of flow characteristics under various operational conditions. The development of advanced CFD software, such as OpenFOAM and ANSYS Fluent, has facilitated the simulation of complex geometries and transient flow phenomena with high precision [40].

Recent advancements include high-performance computing (HPC) techniques, which allow for the simulation of large-scale, three-dimensional flows in a fraction of the time previously required. These advancements enable detailed parametric studies and optimization of pump designs for better efficiency and performance.

2.2.2 Turbulence Modeling

Turbulence modeling is a critical aspect of accurately simulating the flow within centrifugal pumps. Traditional models, such as the $k - \varepsilon$ and $k - \omega$ models [47, 46], provide a good balance between accuracy and computational cost. However, they often struggle to capture the complex flow structures and unsteady phenomena in pump flows.

Recent advancements in turbulence modeling include the development and application of Large Eddy Simulation (LES) and Detached Eddy Simulation (DES) techniques. LES provides a more detailed representation of turbulent flows by resolving the large eddies directly and modeling the smaller scales. This approach offers a significant improvement in capturing the intricate flow features and transient behavior in pumps. DES combines the advantages of both RANS (Reynolds-Averaged Navier-Stokes) and LES by switching between them based on the flow regime, providing an efficient way to simulate complex flows with high accuracy.

2.2.3 Influence of RANS Turbulence Models

Wang et al. [9] performed RANS steady-state simulations applying the Frozen Rotor Method in six and five centrifugal pumps at design conditions, with specific speeds ranging from 34.3 to 260.5. The aim was to study the influence of turbulence models on the head and efficiency. Cavitation was considered by implementing a homogeneous multiphase model. After comparing with experimental data it was concluded that, for low and medium-specific speed pumps, the $k-\omega$ and SST $k-\omega$ models are more suitable while for high specific speeds the $k-\varepsilon$ is prefered than the two other.

Several authors tried to understand the influence of the two-equation turbulence model on the performance of medium-speed centrifugal pumps in design and off-design conditions. Wang and Wang [10] and Nocente et al. [11] applied $k-\varepsilon$, RNG $k-\varepsilon$, Realizable $k-\varepsilon$, $k-\omega$, SST $k-\omega$ and on low specific speed pump ($n_s = 13.6$ and $n_s = 8.6$ respectively); Huang et al. [12] applied $k-\varepsilon$ and the SST$k-\omega$ for a medium specific speed pump ($n_s = 65$); Xianfang et al. [13] applied the $k-\varepsilon$, RNG $k-\varepsilon$, $k-\omega$ and SST $k-\omega$ for a high specific speed pump ($n_s = 140$). Steady-state and transient simulations were performed for all of these works. The frozen rotor method, with the multi-reference frame approach, was applied on the steady state, while the sliding mesh approach was applied on the transient simulations. It was concluded that, for off-design analysis, the SST $k-\omega$ should be applied, as this was the one with a smaller relative error between experimentally measured head, efficiency and power. For design flow rate analysis, either model accurately replicates the experimental data. Since the $k-\varepsilon$ model presents a lower computational time, it should be employed for more efficient analysis, alongside wall functions. Li at al. [14] performed a comparative study for a low specific speed centrifugal pump using five eddy viscosity models and concluded that the $k-\varepsilon$ was the most suitable to compare with design conditions and external characteristics (head, efficiency, power). Wang et al. [15] utilized the $k-\varepsilon$ and SST $k-\omega$ turbulence models to capture the cavitation detachment process. It was noted that, instead of a detachment, the flow steadily attaches on the leading edge of the blades. The SST model is able to capture some unsteady cavity structures. This is explained by the over-prediction of the eddy viscosity in the multiphase region. Wang et al. [9] concluded that, for $n_s < 94.1$, the SST $k-\omega$ turbulence model most accurately predicted the NPSH, while for higher specific speeds, the $k-\varepsilon$ model did. Cheah et al. [16] studied the behaviour of the $k-\varepsilon$ model for design and off-design conditions ($0.43Q_d$ and $1.45Q_d$). For the design flow rate, the impeller passage is smooth, following the curvature of the blade. However, for off-design conditions, flow separation is observed at the leading edge due to non-tangential inflow condition, which is the reason for the unsuitableness of the $k-\varepsilon$ in off-design conditions, since this model is not capable of accurately handling strong adverse pressure gradients. Steady-state analysis is considered suitable if the goal of the study is to predict the overall performance of the pump. Nonetheless, if local perturbations are of utmost importance for the researcher, employing a transient analysis is advised.

2.2.4 Influence of Inducer in Impeller

Work regarding the study of rocket centrifugal pumps has also been developed, mostly associated with cavitation. Hong et al. [17] performed experimental and numerical studies in order to evaluate the impact of usage of inducer on a centrifugal pump in water environment. The Reynolds Averaged method alongside the $k - \varepsilon$ turbulence model with wall functions successfully replicated the experimental results. It is important to note that all the tests and simulations were performed for the design flow rate. It was concluded that the inducer had negligible effect on the head and efficiency of the pump, but a significant effect on the cavitation performance. Yang et al. [18] adopted the Detached Eddy Simulation method to evaluate the influence of the clocking effect between inducer and impeller on a 18000 rpm centrifugal rocket turbopump. If there is misalignment or improper clocking between the inducer and impeller, it can lead to flow disruptions, uneven loading on the impeller, and increased hydraulic losses. These effects can result in reduced pump efficiency, cavitation, or even pump instability, which are highly undesirable in rocket propulsion systems where precision and reliability are paramount (Gülich [6]). A maximum relative error of 2.73% was achieved for the efficiency at the design flow rate. However, that error triplicated in off design conditions ($0.6Q_d$).

2.2.5 Boundary Conditions

Marigorta et al. [19] and Spence and Amaral-Teixeira [20] discuss about the three most usual combinations of boundary conditions used in centrifugal pumps analysis: (1) inlet - total pressure, outlet - mass flow (2) inlet - mass flow, outlet - static pressure (3) inlet - total pressure, outlet - static pressure. Marigorta et al. [19] utilized the second set of boundary conditions, despite suggesting that combination number three would provide the most accurate results. It is also observed that the choice of boundary conditions can speed up numerical convergence. Marigorta et al. [19] indicates that five impeller revolutions are needed in order to achieve periodic unsteady solution convergence. Later work by Gonzalez et al. [21], [22] indicates that, utilizing the third set of boundary conditions, and initializing the transient simulation with results from steady state numerical calculations, ten impeller revolutions are needed instead. Spence and Amaral-Teixeira[20] conducted analysis with each set and found that, despite the third set providing more accurate results, the losses of accuracy when compared to the second set are minor. Furthermore, Spence and Amaral-Teixeira agree that the second set is significantly more stable and converged faster.

2.2.6 Steady State vs Transient

Mentzos et al. [23] carried out steady state simulations adopting the Multi Reference Frame approach. The main goal was to study the impeller-volute interaction, which com-

pletely failed. Nevertheless, a steady state analysis was still sugested as a tool for a basic understanding of the flow at various operating points, as well as an initial solution for transient calculations. Wang and Wang [10] performed steady calculations on five different turbulence models, and good agreement with experimental data was achieved for design flow rate. For off-design, every model showed a considerable deviation. If the start phase is of no interest for the study, a steady state solution is usually utilized as the initial field for pressure, velocity and the turbulent constants for a transient analysis [24]. The Multi Reference Frame approach can only be applied to a steady state simulation. Dick et al. [1] utilized the Multi Reference Frame and the Mixing Plane approaches for steady state simulations, and the Sliding Mesh approach for unsteady simulations. It was found that steady state approaches lead to completely erroneous flow field predictions for flows far away from the design flow rate. Furthermore, the angular position of the impeller affects the results in steady state analysis.

2.2.7 Grid and Time Independence

It is an fundamental practice to verify that the results do not depend on the numerical grid utilized for the domain discretization.

Wang et al. [9] studied the influence of residual target on the precision of predicted results, by using the $k-\varepsilon$ turbulence model. Between 10^{-4} and 10^{-5}, the run time increased around two times for every simulation, and the predicted results did not change more than 0.75%. A residual criteria of 10^{-4} was selected for steady state analysis. Several other authors agree with this procedure [25], [26], [27], [20]. For transient simulations, residuals are usually kept between 10^{-5} [22] or 10^{-6} [12].

Regarding domain discretization, Wang et al. [9] decided that it was achieved when the effect of grid number on pump characteristic parameters changed no more than 0.1%. Alemi et al. [25] grid changed no more than 0.8% the results from the previous grid. Fu et al. [28] achieved grid convergence when the results did not change more than 0.06 % from the previous iteration.

When it comes to temporal discretization, the turbomachinery community usually defines the time step in either one or more of the following: time step in seconds, number of time steps per impeller rotation and number of degrees rotated per time step. Spence and Amaral-Teixeira [20], [29] performed 288 time steps, which corresponds to 1.25°per time step, and 250 time steps per impeller rotation in the respective mentioned papers. The Courant-Freidrich-Levy number is kept less then 30. Bai et al. [26] defines a time step corresponding to 1°of impeller rotation (1.149×10^{-4}). Li et al. [30] selected a fixed time step of 1×10^{-4} for the study of a centrifugal pump during startup. Gonzalez et al. [21] used a time step of 2.703×10^{-4} and kept a CFL below 3. [11] 0.484 °5.5×10^{-5}, . Huang et al. [12] performed numerical studies in OpenFOAM and set the time step to 5×10^{-5} s, the equivalent to 1°rotation, keeping the CFL below 5.

2.2.8 Impeller-Volute Interaction

The relative movement between impeller and volute generates an unsteady interaction which affects not only the overall pump performance but is also responsible for pressure fluctuations. Pressure fluctuations interact with the volute casing and give rise to dynamic effects (mainly unsteady forces) over the mechanical parts, which are one of the most important sources of vibration and hydraulic noise. Dick et al. [1] portraits the impact that the natural unsteadiness in a centrifugal pump with a tonged volute has in the overall pump head. It is suggested that several impeller radial positions should be adopted in a steady calculation. Gonzalez et al. [22] concluded that an unsteady RANS analysis could accurately predict pressure fluctuations, as well as dynamic forces which can cause fatigue failure of the pump axis [8].

2.2.9 Emerging Trends and Future Directions

Emerging trends and future directions in centrifugal pump technology are shaped by advancements in materials science, computational modeling, and environmental considerations. Researchers are focusing on improving the efficiency and reliability of these pumps through the development of new materials that can withstand harsh operating conditions, such as high temperatures and corrosive environments. For instance, the use of advanced composites and ceramics can significantly enhance the durability and performance of centrifugal pumps used in critical applications like rocket engines and chemical processing [31, 32].

Another promising direction is the use of additive manufacturing techniques, such as 3D printing, for the production of complex pump components. This technology allows for the fabrication of highly customized designs with intricate internal geometries that are difficult to achieve with traditional manufacturing methods, leading to improved pump performance and reduced costs [33].

Moreover, the integration of computational fluid dynamics (CFD) and advanced simulation techniques has revolutionized the design and optimization of centrifugal pumps. These tools allow engineers to predict and analyze the internal flow characteristics under various operating conditions, leading to more efficient and tailored designs. Studies have demonstrated that optimizing the startup and operational parameters can significantly reduce energy losses and improve overall system efficiency [31].

In conclusion, the field of centrifugal pump research is rapidly evolving, driven by advancements in computational modeling, materials science, and digital technology. These innovations are paving the way for more efficient, reliable, and cost-effective pump designs, with significant implications for a wide range of industrial applications. In Table 2.1, a comparison of various CFD methodologies from different studies is displayed, highlighting the turbulence models, cavitation modeling approaches, and discretization

schemes applied in the analysis of centrifugal pump flow characteristics.

Table 2.1: Comparison of CFD Methodologies in Various Studies for Modeling Flow Characteristics.

Authors	Time	Flow Rate Range ($\times Q_d$)	Turbulence Models[a]	Cavitation Modeling	Convective Terms Discretization	Diffusive Terms Discretization	Temporal Discretization	Boundary Conditions	CFL	Specific Speed
Wang et al. [9]	Steady	1	$k-\varepsilon$, $k-\omega$ SST $k-\omega$ $l_t = 0.07D_{inlet}$	Homogeneous multiphase model Rayleigh-Plesset for evaporation and condensation	High-resolution	Central differencing	-	Inlet: total pressure Outlet: constant mass flow rate	-	$34.3 \sim 260.5$
Huang et al. [12]	Steady and Transient	$0.3 \sim 1.4$	Transient: URANS Steady: RANS $k-\varepsilon$, SST $k-\omega$	No cavitation	Linear Upwind	Linear	-	Inlet: fixed velocity Outlet: fixed pressure	5, 5×10^{-5}, 1°	65
Wang and Wang [10]	Steady	$0.3 \sim 1.7$	$k-\varepsilon$, $k-\omega$ SST $k-\omega$, RNG $k-\varepsilon$ Realizable $k-\varepsilon$	No cavitation	Central Differencing Second Order	Central Differencing Second Order	-	Inlet: fixed velocity Outlet: fixed pressure	-	12.98
Alemi et al. [25]	Steady	$0.825 \sim 1.12$	$k-\varepsilon$, $k-\omega$ SST $k-\omega$ $I = 5\%$, $\mu_t/\mu = 10\%$	No cavitation	Second Order Upwind	Second Order Upwind	-	Inlet: constant mass flow rate Outlet: fixed pressure	-	21
Fu et al. [28]	Steady	$0.4 \sim 1.2$	$k-\varepsilon$	Rayleigh-Plesset Equation	High Resolution Scheme	High Resolution Scheme	-	Inlet: fixed pressure Outlet: constant mass flow rate	-	66
Shojaeefard et al. [24]	Steady	$0.5 \sim 1.5$	SST $k-\omega$	No cavitation	-	-	-	Inlet: fixed pressure Outlet: constant mass flow rate	-	23.65
Bai et al. [26]	Steady and Transient	$0.8 \sim 1.2$	URANS SST $k-\omega$ $I = 5\%$	No cavitation	-	-	-	Inlet: fixed total pressure Outlet: constant mass flow rate	1°per iter	29.5
Li et al. [30]	Steady and Transient	-	Steady: Realizable $k-\varepsilon$ Transient: DES		Second Order Upwind	Central Differencing	-	Closed Domain No inlet or outlet	0.001	57.6
Gonzalez et al. [22]	Transient	-	URANS $k-\varepsilon$		Second Order Upwind	Central Differencing	Second Order Implicit	Inlet: total pressure Outlet: static pressure proportional to the velocity	< 3, 2.703×10^{-4}s	29.18
Wang et al. [15]	Transient	-	SST $k-\omega$ $k-\varepsilon$	Schnerr-Sauer [34]	-	-	-	Inlet: pressure Outlet: mass flow	3°per iter, $T/120$	37.03
Mousmoulis et al. [27]	Steady	-	SST $k-\omega$	Zwart et al. [35]	Second Order	Second Order	-	Inlet: mass flow Outlet: static pressure	-	12.30
Auvinen et al. [36]	Transient	1	SST $k-\omega$	-	Second Order, Linear	Second Order, Linear	-	Inlet: mass flow Outlet: static pressure	0.5°per iter	46.39
Spence and Amaral-Teixeira [20]	Transient	$0.25 \sim 1$	$k-\varepsilon$	No cavitation	-	-	First order	Inlet: mass flow Outlet: static pressure	25-30, 1.25° per time step 1.488×10^{-4}	26.31

Chapter 3

Mathematical Model

3.1 Reynolds Number

The Reynolds number, Re, is a dimensionless number that represents the ratio of inertial forces and viscous forces acting on the body [37]. It is given by Equaion (3.1), where ρ is the fluid density, U_∞ is the free stream velocity, L is the characteristic length and μ is the dynamic viscosity. It also indicates if the flow is laminar or turbulent. A high Re means that inertial forces are dominant over viscous forces. As mentioned in the previous paragraph, boundary layers can be laminar or turbulent. No exchange between the individual streamlines takes place in a laminar flow, apart from molecular diffusion. However, mixing movements perpendicular to the flow occur in turbulent flow. The presence of eddies of finite magnitude ensures lateral transport. The reason why turbulent boundary layers typically have a later flow separation is the increased momentum carried by them [6].

$$\mathrm{Re} = \frac{\rho U_\infty D}{\mu} \quad (3.1)$$

In turbopumps, the Re in the major part of the fluid domain is so high that the flow is undoubtedly turbulent. Dixon [3] states that, for $\mathrm{Re} > 2 \times 10^5$, the effects of Re on the performance of turbomachines is small, since the viscous boundary layers on the blades of a turbomachine are generally turbulent and very thin. Dixon [3] also states that, for turbopumps handling water, the kinematic viscosity, $\nu = \mu/\rho$ is low, and the corresponding Re number is so high that its effects may be ignored in a first approximation. However, Omnidea, Lda's. main goal is to achieve the most detailed flow results possible and since the consideration of viscosity in the calculations does not significantly increase the computational time it will be considered.

The Re can also be written as a function of the distance from the wall, y, given by Equaion (3.2). When y is large, Re_y will also be larger, meaning that the inertial forces will dominate over the viscous. However, if the value of y tends to zero, meaning a closer distance to the wall, the viscous forces will dominate.

$$\mathrm{Re}_y = \frac{\rho U_\infty y}{\mu} \quad (3.2)$$

This led to the non-dimensional wall distance y^+, described in Equaion (3.3) , where u^* is

termed the friction velocity because it has dimensions LT^{-1}, although it is not actually a flow velocity[38]

$$y^+ = \frac{\rho y u^*}{\mu} \qquad u^+ = \frac{u}{u^*} \qquad u^* = \sqrt{\tau_w/\rho} \quad (3.3)$$

3.1.1 Dimensionless Wall Distance, y^+ and Wall Functions

In the 20th century, fluids with different properties were used to measure, at different velocities, the velocity profile in a pipe flow and it was found out that a relation between y^+ and u^+ was present in all of the experiments [37] . The several results can be summarized by the solid line in Figure 3.1.

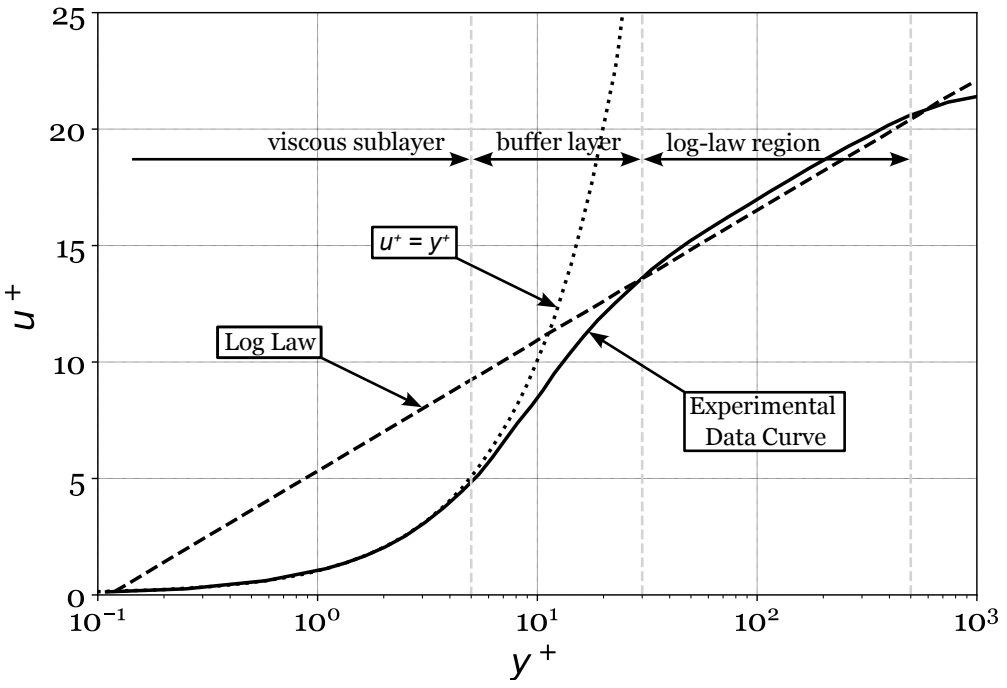

Figure 3.1: Experimental data curve obtained from the several experiments performed in the last century and relation with the Logarithmic Overlap Law (or Log Law). Adapted from [38]

As displayed, the boundary layer is divided in two main regions. The inner layer and the outer layer. This inner layer is subdivided in three regions:

- viscous sublayer ($y^+ < 5$), which is dominated by viscous stresses. This region is accurately defined by the linear relation $y^+ = u^+$;
- buffer layer ($5 \leq y^+ \leq 30$), where the presence of viscous and turbulent stresses is of similar weight. The linear approximation $u^+ = y^+$ causes departures from accurate

results of at least 25% for $y^+ > 12$ according to [39];

- log-law region ($y^+ > 30$), where the turbulent stresses prevail. This region is accurately defined by the following relation:

$$u^+ = \frac{1}{\kappa} \ln y^+ + B \quad (3.4)$$

where κ is the von-Kármán constant and B is a constant. There is some variation regarding these values, but generally they are within 5% of $\kappa = 0.41$ and $B = 5.2$ [39]. This is the so called law of the law of the wall and is due to Von-Kármán.

In CFD, the variation of velocity, temperature, pressure, etc. across cells in the mesh is linear. The main goal of a CFD analysis is, most of the time, to analyze how a body affects a flow field (external flow), or how the flow behaves inside a solid (internal flow). Either it is an internal or external analysis, there is a region close to the wall of the bodies where the velocity gradients are steep, which is called the boundary layer. This would require the usage of extremelly thin cells to resolve the velocity profile, increasing the cell count thus the necessary computational power.

However, as seen in Figure 3.2, if the mesh is too coarse, the velocity distribution will not be accurately captured, leading to significant errors in the CFD results. This is due to the fact that the wall shear stress, τ, directly depends to the velocity gradient, as described in Equaion (3.5), where μ is the dynamic viscosity, u is the velocity magnitude and y is the wall distance.

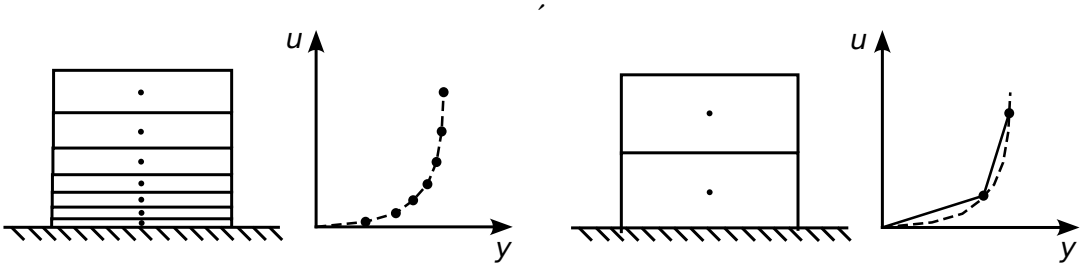

Figure 3.2: (a) Refined wall mesh region and respective velocity distribution versus (b) coarser mesh with real velocity distribution (dashed line) and captured velocity distribution (solid line).

$$\tau = -\mu \frac{\partial u}{\partial y} \quad (3.5)$$

Nevertheless, if the cells near the wall are kept in a dimension so that $30 < y^+ < 500$, according to [40], it is possible to use the log-law, which will significantly decrease the

computational cost. It is important to note that wall functions are only applied to the first layer of cells.

3.2 Conservation Laws

Conservation of mass, momentum and energy completely defines all the fluid flows. A total of five equations are represented, as the momentum, defined as the product of density and velocity, is a tridimensional vector in space. It is important to note that not all quantities satisfy the conservation law. It is the case for pressure, temperature, and entropy, for instance. However, there are equations that define these quantities, just not in the form of a conservation law [41].

The method outlined in this research addresses the challenges within continuum mechanics. The length and time scales for these issues are notably larger than the scales of the material's discrete structure. Hence, it becomes feasible to represent any overall physical property of the material as a continuous function in macroscopic coordinates such as time and space.

3.2.1 Mass Conservation Equation

The conservation of mass states that in a fluid system, mass cannot either be created or destroyed. No diffusive flux exists for the mass transport, which means that mass can only be transported through advection. In the absence of external mass sources, the mass conservation equation, also known as the continuity equation, can be written in its integral form such as in Equation (3.6).

$$\underbrace{\frac{\partial \rho}{\partial t}}_{\text{Rate of Increase of } \rho} + \underbrace{\nabla \cdot (\rho \vec{u})}_{\text{Advective Term}} = 0 \quad (3.6)$$

where the first term represents the rate of increase of ρ, and the second term represents the amount of ρ that is transported by the fluid. It is also known as the advective term in the mass conservation equation. If the fluid is incompressible, Equation (3.6) is reduced to Equation (3.7), the divergence free condition for the velocity.

$$\nabla \cdot \vec{u} = 0 \quad (3.7)$$

3.2.2 Momentum Conservation Equation

The momentum equation is, fundamentally, Newton's second Law applied to fluid mechanics. It states that the rate of change of momentum of a fluid particle equals the sum of forces acting on the particle [40]. It is defined by Equation (3.8).

$$\underbrace{\frac{\partial \vec{u}}{\partial t}}_{\text{Rate of Increase of ũ}} + \underbrace{(\vec{u}\cdot\nabla)\vec{u}}_{\text{Advective Term}} = \underbrace{\frac{1}{\rho}\left(-\nabla p + \nabla\cdot\bar{\bar{\tau}}\right)}_{\text{Diffusive Term}} + \underbrace{\vec{f_e}}_{\text{External Forces}} \quad (3.8)$$

where $\bar{\bar{\tau}}$ is the shear stress tensor defined by Equation (3.9).

$$\bar{\bar{\tau}} = \mu\left(\nabla\vec{u} + (\nabla\vec{u})^T\right) - \frac{2}{3}(\nabla\cdot\vec{u})I \quad (3.9)$$

As seen in the equation above, the diffusive term depends now on the kinematic viscosity of the fluid, ν, due to surface forces. Internal forces cancel each other inside the volume Ω due to Newton's Third Law of Motion. However, this does not happen on the surface S, since there is no counter action. Thus, surface and pressure forces must be accounted on the momentum equation.

If the flow is incompressible, with a constant viscosity and satisfies the divergence free velocity condition (Equation (3.7)), Equation (3.8) can be rewritten in a simplified form presented in Equation (3.10).

$$\frac{\partial \vec{u}}{\partial t} + (\vec{u}\cdot\nabla)\vec{u} = -\frac{\nabla p}{\rho} + \nu\nabla^2\vec{u} + \vec{f_e} \quad (3.10)$$

3.2.3 Conservation Equations in Moving Reference Frame

Turbomachinery problems will require the conservation equations to be written in a rotating frame. Thus, a relation between the inertial frame and the rotating frame needs to be imposed. The following relations are retrieved from Buchmayr [42]. In order to define the velocity in an inertial frame, it is necessary to establish a relation between the velocity in a rotating frame, as in Equation (3.11)

$$\vec{u}_I = \vec{u}_R + \vec{\omega}\times\vec{r} \quad (3.11)$$

where $\vec{u}_I$ and $\vec{u}_R$ are the velocity fields relative to the inertial and rotating systems, respectively, $\vec{\omega}\times\vec{r}$ is the entrainment velocity and $\vec{r}$ is the position vector.

The entrainment velocity does not contribute to the mass balance, so the mass conservation equation will remain invariant, and can be written directly in the relative system, as

in Equation (3.12).

$$\frac{\partial \rho}{\partial t} + \nabla \cdot (\rho \vec{u_R}) \quad (3.12)$$

The momentum equation can be written as in Equation (3.13)

$$\frac{\partial \vec{u}_R}{dt} + \frac{d\vec{\omega}}{dt} \times \vec{r} + \underbrace{2(\vec{\omega} \times \vec{u}_R)}_{\text{Coriolis Force}} + \underbrace{\vec{\omega} \times (\vec{\omega} \times \vec{r})}_{\text{Centrifugal Force}} + \underbrace{(\vec{u_R} \cdot \nabla)\vec{u}_R}_{\text{Advective Term}} = \underbrace{-\frac{\nabla p}{\rho} + \nu \nabla^2 \vec{u}_R}_{\text{Diffusive Term}} + \underbrace{\vec{f_e}}_{\text{Body Forces}} \quad (3.13)$$

However, for steady state solvers in OpenFOAM, the momentum equation is formulated for the absolute velocity. Hence, Equation (3.13) can be further developed so the advected velocity is the velocity in the inertial frame, as in Equation (3.14).

$$\frac{\partial \vec{u}_R}{dt} + \frac{d\vec{\omega}}{dt} + (\vec{u_R} \cdot \nabla)\vec{u}_I + (\vec{\omega} \times \vec{u}_I) = -\frac{\nabla p}{\rho} + \nu \nabla^2 \vec{u}_I \quad (3.14)$$

This is the momentum conservation equation used in steady state solvers. It can only be used within static volumes.

3.3 Approximations

The conservation laws are nonlinear equations. The presence of nonlinearity in the flow formulas is not just a mathematical aspect. It significantly impacts fluid mechanics as a whole: The most influential nonlinearity emerges from the advection term $(\vec{u} \cdot \nabla)\vec{u}$, evident in the momentum conservation equation, as shown in Equation (3.10). This specific term induces turbulence, an abrupt instability in the flow that leads to all variables exhibiting a statistical (chaotic) behavior [41].

In order to solve or model turbulence, three main methods have been developed up to date. Direct Numerical Simulation (DNS) solves all eddy scales. Domains must be temporally and spatially discretized in order to capture the Kolmogorov Scale. The DNS method is not used in engineering applications due to its demanding computational resources. Large Eddy Simulation (LES) is similar to DNS. The main difference is that it solves only larger scales, while the smaller scales (subgrid scales) are modeled. The time needed to perform LES simulations is significantly smaller than DNS, however it is still excessively high for higher Reynolds number applications. A domain where LES is coming to pratical industrial engineering applications is the modeling of combustion phenomena [41]. The

most widely applied applied method for modeling turbulence is the Reynolds Averaging, which is going to be looked into in the next section.

3.3.1 Reynolds Averaged Navier-Stokes Equations (RANS)

Reynolds Unweighted Averaging is a statistical approach, where it is assumed that the local value of the quantity ϕ can be separated into a mean value, $\overline{\phi}$, and a fluctuation of that same variable, ϕ', (Jasak [43]), as presented in Equation (3.15).

$$\phi(t,\vec{r}) = \overline{\phi}(t,\vec{r}) + \phi'(t,\vec{r}) \quad (3.15)$$

When time averaging the set of conservation laws (Equations (3.6) and (3.8)) can be rewritten as in Equation (3.16)

$$\begin{cases} \dfrac{\partial \rho}{\partial t} + \nabla \cdot (\rho \overline{\vec{u}}) = 0 \\ \\ \dfrac{\partial \overline{\vec{u}}}{\partial t} + (\overline{\vec{u}} \cdot \nabla)\overline{\vec{u}} = \dfrac{1}{\rho}\left(-\nabla \overline{p} + \nabla \cdot \overline{\overline{\tau}} + \nabla \cdot \overline{\overline{\tau}}'\right) + \vec{f_e} \end{cases} \quad (3.16)$$

where a new term designated as Reynolds Stress Tensor, $\overline{\overline{\tau}}'$ arises. It can be defined in Equation (3.17).

$$\overline{\overline{\tau}}' = -\overline{\rho \vec{u}' \vec{u}'} \quad (3.17)$$

The Reynolds Stress Tensor introduces a closure problem, since there are now more unknown variables than equations in the system. In order to close the system, further modeling is necessary. There are two commonly embraced methods. The first one involves establishing and resolving the transport equation for the Reynolds stress tensor. The second and most popular approach is using the Boussinesq approximation [44]. It defines that the the Reynolds Stress Tensor can be defined as in Equation (3.18).

$$-\overline{\rho \vec{u}' \vec{u}'} = \mu_t(\nabla \vec{u} + (\nabla \vec{u})^T) + \frac{2}{3} k \vec{I} \quad (3.18)$$

where μ_t is the turbulent viscosity and k is the turbulent kinetic energy defined in Equation (3.19).

$$k = \frac{1}{2}\left(\overline{u'^2} + \overline{v'^2} + \overline{w'^2}\right) \quad (3.19)$$

With this approximation, turbulence models are now applied to calculate μ_t and k

3.4 Turbulence Modelling

The choice of a turbulent model in order to resolve the turbulent viscosity is an essential task in every Reynolds Averaged problem. As mentioned before, the Reynolds Stress Tensor can be directly solved. However, the focus is to model it by using Boussinesq's approximation.

As of today, several turbulence models have been developed. They approach the closure problem in different ways, but generally using the same properties such as the turbulent kinetic energy, k, the turbulent dissipation rate, ε, and the turbulent specific dissipation rate, ω. No model produces consistent outcomes for a range of Reynolds numbers, free-stream turbulence levels, and pressure gradients. The results are influenced by factors such as initial conditions, boundary conditions, and numerical parameters, including grid resolution and the extension of the computational domain [45]. Alemi et al. [25] found a value of 5% for the turbulent intensity, I, and eddy viscosity ratio, μ_t/μ, of 10 suitable for applying in a low specific speed centrifugal pump.

3.4.1 Standard $k-\varepsilon$

The standard $k-\varepsilon$ model which is implemented in OpenFOAM is based on the modified model proposed by Launder and Spalding in 1974 [46]. The authors define an equation for the turbulent mixing lenght, l_t, which represents the macroscale of turbulence, defined in Equation (3.20).

$$l = \frac{C_m u k^{3/2}}{\varepsilon} \quad (3.20)$$

This definition might be questionable, since it uses the "small eddy" variable ε to define the larger eddy scale l_t. We are allowed to do this because, at high Reynolds numbers, the rate at which large eddies draw energy from the mean flow is generally balanced by the rate at which energy is transferred across the energy spectrum to smaller, dissipating eddies, assuming the flow changes gradually. If this balance did not exist, the energy at certain turbulence scales could either increase or decrease indefinitely.

$$\mu_t = C_\mu \rho k^{1/2} l \quad (3.21)$$

With this, it is possible to write two equations, for each of the variables k and ε, presented in Equations (3.22) and (3.23) respectively.

$$\frac{Dk}{Dt} = \frac{1}{\rho}\frac{\partial}{\partial x_k}\left[\frac{\partial \mu_t}{\partial x_k}\frac{\partial k}{\partial x_k}\right] + \frac{\mu_t}{\rho}\left(\frac{\partial U_i}{\partial x_k} + \frac{\partial U_k}{\partial x_i}\right)\frac{\partial U_i}{\partial x_k} - \varepsilon \quad (3.22)$$

$$\frac{D\varepsilon}{Dt} = \frac{1}{\rho}\frac{\partial}{\partial x_k}\left[\frac{\mu_t}{\sigma_\varepsilon}\frac{\partial \varepsilon}{\partial x_k}\right] + \frac{C_1 \mu_t}{\rho}\frac{\varepsilon}{k}\left(\frac{\partial U_i}{\partial x_k} + \frac{\partial U_k}{\partial x_i}\right)\frac{\partial U_i}{\partial x_k} - C_2\frac{\varepsilon^2}{k} \quad (3.23)$$

The constants of the model are listed in Table 3.1.

Table 3.1: Standard $k - \varepsilon$ model constants. Launder and Spalding [46]

Constant	Value
C_μ	0.09
C_1	1.44
C_2	1.92
σ_k	1.0
σ_ε	1.3

This turbulence model main drawbacks are the over-prediction of the turbulent kinetic energy at stagnation points and inaccuracy at predicting boundary layers with adverse pressure gradients.

Chapter 4

Finite Volume Discretization

In order to solve the fluid dynamics partial differential equations, they must be transformed into a corresponding system of algebraic equations. As of today there are three main methods to discretize the space derivatives in the conservation laws. The Finite Difference Method, FDM, which remains a reference for all studies of numerical discretization, is the most traditional and oldest method. However, it can only be applied in practice to structured grids. The Finite Element Method, FEM, is mostly applied to structural mechanics, and due to the lack of scientific research on that method, this Master's dissertation will make use of the third and most popular method: the Finite Volume Method, FVM, which discretizes directly the integral form of the conservation laws. Its popularity arises due to its generality, conceptual simplicity and possibility of appliance to unstructured grids (Hirsch [41]).

According to Jasak [43], the FVM has the following properties:

- The method is based on discretizing the integral form of governing equations over each control volume. Therefore, the basic quantities will therefore be conserved at the discrete level.

- Jasak states that equations are solved in a fixed Cartesian coordinate system on a static grid. However, it is now possible to derive the governing equations in a moving reference of frame, as well as to apply the sliding mesh method in order to solve moving domains (Buchmayer [42]).

- The control volumes can assume a polyhedral shape and are able to assume an unstructured mesh domain.

- Systems of partial differential equations are solved one at a time, with inter-equation coupling treated in the explicit manner, as is the case of the SIMPLE, PISO and PIMPLE algorithms, that are going to be discussed in a further section. Non-linear differential equations are linearized before the discretization.

The discretization process can be divided into two steps: the discretization of the solution domain and equation discretization. Moreover, the solution domain discretization can further be split into discretization of time and space.

4.1 Discretization of the Solution Domain

The first step on the discretization of the solution domain is the space discretization. It is necessary both for steady and unsteady numerical analysis. In Figure 4.1 is presented a typical control volume. The computational point P is located at the centroid of the control volume [43], such that:

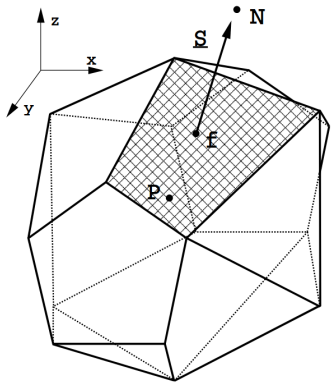

Figure 4.1: Polyhedral control volume [43].

The mean value of every value at each point inside a control volume is projected to the centroid of thee volume. This approximation is known as the ”Mean Value Theorem”, and is second order accurate (Buchmayr [42]). The set of control volumes fulfilling the domain composes the domain grid.

4.1.1 Grid Properties

Grid generation is a major component in setting up a CFD simulation (Hirsch [41]). Grids can be distinguished between structured and unstructured, each one having its advantages and disadvantages Structured Grids are considered more natural if aligned with the flow, computationally more efficient in terms of accuracy, CPU time and memory requirement. However, it is harder to add boundary layer grid points, and if a local refinement is necessary. The addition of a point implies adding lines of each family through that point, affecting the whole domain (Hirsch [41]). Unstructured Grids can easily adapt to complex geometries, interact well with the concept of local refinement, where points are added locally without disturbing the rest of the mesh and require significantly less time to generate than structured grids. However, they tend to have a lower accuracy than the corresponding structured grid. Nevertheless, the scientific community has lately been adopting an unstructured or hybrid grid approach and accurate results were achieved [9] [12] [10] [25] [28] [24] [30] [22] [27].

It is important to mention that the same computational domain can be split into structured and unstructured grids, as seen in Figure 4.2. In a geometrically simpler region,

where it is known that the flow is going to travel parallel to one of the components of the cartesian axis, a structured mesh approach is adopted. In rotating regions, where a less predictable flow may arise, an unstructured tetrahedral mesh is adopted. However, this hybrid approach requires a treatment in order to compute the fluxes between non coupling cell faces. The same treatment is necessary in dynamic meshes. Usually the Adaptative Mesh Interface, AMI, approach is adopted. However, OpenFOAM v11 developers replaced it by the Non Conformal Coupling, NCC [49]. It is an improvement which allows its usage on partially plane or curved overlapping patches, and it presents an increase in accuracy on the global imbalance.

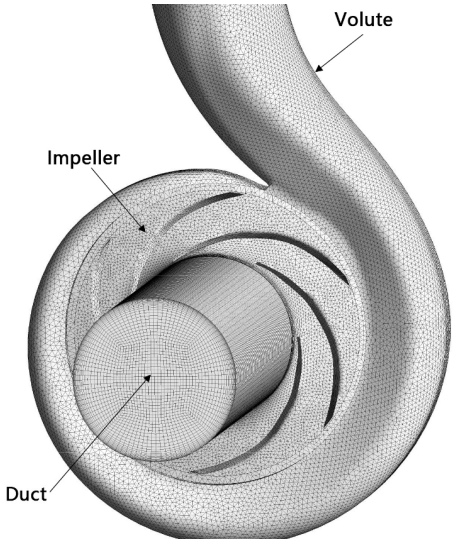

Figure 4.2: Unstructured and structured grids used in the same computational domain [12].

4.1.2 Orthogonality

Orthogonal grids are the optimal ones in the field of computational fluid dynamics. They grant that the numerical discretization scheme remains with the original accuracy order. That is, a second order scheme will remain second order accurate in an orthogonal mesh. However, these meshes are not usually used in engineering applications since geometries require the presence of a non-orthogonal angle in order to accurately capture the domain. Mesh orthogonality is the angular deviation of the vector $\vec{S}$ (located at the face center f) from the vector $\vec{d}$ connecting the two cell centers C and D. In Figure 4.3 is displayed the graphical representation of the non-orthogonal angle. The OpenFOAM user guide [50] suggests that a maximum non-orthogonal angle, θ, of 85° should be employed. If it surpasses that value, a new mesh should be created. However, a value of $60 < \theta < 75$ is recommended for accurate results.

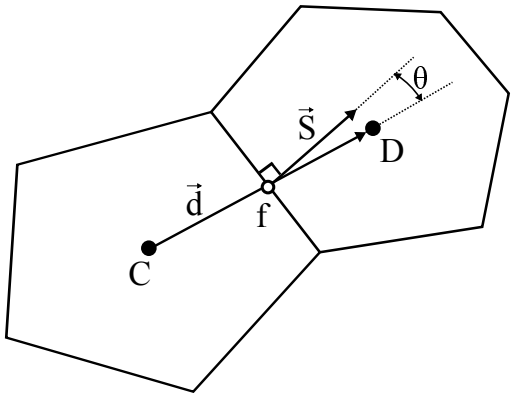

Figure 4.3: Mesh non-orthogonality.

4.2 Discretization of the Transport Equations

During this work, the transport equations will be solved considering an incompressible flow and a rotating frame of motion. The mass conservation and momentum conservation equations are presented in Equation (3.12) and Equation (3.14), respectively. The first one is a first order equation, while the later one is a second order equation due to the diffusion term. According to Jasak [43], in order to keep a good accuracy of the solution, a dizcretization method of equal or higher order than the order of the equation that is being discretized must be employed, either on space and time. During this work no time discretization methods will be employed since the temporal derivative will not be present in either of the governing equations.

OpenFOAM utilizes a cell-centered approach. This means that the calculated variables and their quantities are stored at the centroids of the grid cells. In a vertex-centered approach, these variables are stored at the vertices. Thus, the problem of discretizing the advective term in governing equations for a scalar ϕ comes down to finding the value of ϕ at the face f, ϕ_{f}. This scenario is represented in Figure 4.4. Despite being the most widely used method, a cell centered approach presents two main disadvantages [51]. The treatment of non-conjunctional elements and the diffusion term discretization between non-orthogonal cells.

4.2.1 Diffusion Term

The diffusion term present in the momentum equation is characterized by the Laplacian operator, $\nabla^2 f$. It is defined as the divergence, $\nabla\cdot$, of the gradient, ∇f, where f is a twice-differentiable real-valued function.

The discretization of the diffusion term, as well as all the terms where the Laplacian operator is present will be done through a Central Differencing (CD) scheme. It is based on a second-order accurate discretized form of the Guass' theorem, displayed in Equation (4.1).

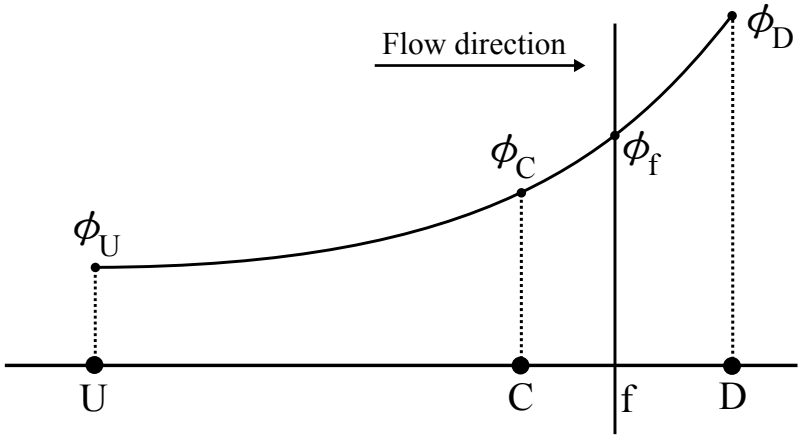

Figure 4.4: Variation of ϕ around the face f. Adapted from [43].

$$(\nabla \cdot \vec{\mathrm{a}}) = \sum_f \vec{\mathrm{S}}.\vec{\mathrm{a}}_f \quad (4.1)$$

Here, $\vec{\mathrm{a}}$, represents a general vector property, f implies the value of a variable in the middle of the face and $\vec{\mathrm{S}}$ is the outward-pointing face area vector which might not be perpendicular to the face. The only choice in OpenFOAM v11 for the interpolation type used to calculate the diffusivity at the face is the linear method, displayed in Equation (4.2).

$$\phi_f = f_x \phi_{\mathrm{C}} + (1 - f_x)\phi_{\mathrm{D}} \quad , \quad f_x = \frac{\overline{f\mathrm{D}}}{\overline{\mathrm{PD}}} \quad (4.2)$$

Discretization methods for the diffusion term strongly depend on the orthogonality of the grid. Most of the grids used in today's application are non-orthogonal, that is, the fluxes are not normal to the cell faces. Thus, an approach needs to be chosen. Typically, the normal vector $\vec{\mathrm{S}}$ is split into an orthogonal and a non-orthogonal contribution, as shown in Equation (4.3).

$$\vec{S}.(\nabla\phi)_f = \left|\vec{\Delta}\right| \frac{\phi_{\mathrm{D}} - \phi_{\mathrm{D}}}{\left|\vec{\mathrm{d}}\right|} + \vec{\mathrm{k}}.(\nabla\phi)_f \quad (4.3)$$

The diffusion term will present a bounded behavior only on orthogonal meshes. The non-orthogonality correction might create unboundness. If the non-orthogonality surpasses a certain threshold, a limiter might be required if stability is more important than accuracy. The OpenFOAM v11 developers suggest that if $\theta > 75°$, a limiter should be applied, and if $\theta > 85°$, convergence might be hard to achieve [50]. All the meshes presented in this work achieved a maximum non-orthogonality, $\theta_{\max} = 65°$, so no limiter is applied.

4.2.2 Advective Term

The advective term is represented by the divergence operator, $\nabla\cdot$. On the contrary of what is observed for the diffusive term, the advective term can be discretized using different schemes in OpenFOAM. The linear interpolation, as shown in Equation (4.2) is second order accurate [52]. Nevertheless, accuracy comes at cost of unstability.

In advection-dominated problems, this central differencing scheme causes nonphysical oscillations which violates the boundness of the solution [43]. In order to counter this phenomena, first order schemes have been introduced, such as the Upwind Differencing (UD). Despite boundness being guaranteed, this comes at the expense of accuracy. The upwind differencing is only first-order accurate, since the value of the property ϕ remains constant between the cell centroid and the cell face. For the purpose of this work, UD was used to generate initial solutions in order to increase stability of the final iterations.

In order to tackle both of the problems introduced by the previous two classes of schemes, authors have been trying to create schemes that are blended between first and second order accuracy and bounded. The Blending Differencing (BD) [53], Second Order Upwind (SOU) [54] and Fromm-based schemes [55] are some of the various attempts to do so. During this work, the Linear Upwind scheme, which is a Fromm-based scheme, will be used for the momentum and mass conservation equations. For an arbitrary grid, the *linearUpwind* scheme implemented in OpenFOAM operates as follows in Equation (4.4).

$$\phi_f = \phi_{\mathrm{C}} + \varphi \cdot (\nabla\phi)_{\mathrm{C}} \cdot \vec{\mathrm{r}} \quad (4.4)$$

The first term on the right hand side (RHS) of Equation (4.4) accounts for the UD part, and the second term on the RHS accounts for the linear part. The main difficulty regarding the *linearUpwind* scheme is related to this gradient. If the gradient on the cell centroid is too steep, it might cause a nonphysical value where the magnitude of ϕ_f is greater than the values of ϕ_{C} and ϕ_{D}. This is why the limiter $0 < \varphi < 1$ is implemented. The implementation of this scheme in OpenFOAM is not this straightforward since several times of limiters are present: *cellMDLimited*, *cellLimited*, *faceMDLimited* and *faceLimited*. Similarly to what happens in Equation (4.4), a coefficient ranging from 0 to 1 is chosen according to the level of boundness that is desired. Contrary to what happens in Equation (4.4), a value of 1 in OpenFOAM corresponds to maximum boundness.

It was mentioned before that the Linear Upwind discretization scheme was used for the momentum and mass conservation equations. Nevertheless, when using a RANS approach, some other scalar properties come into consideration, so does the importance of boundness. For instance, a negative value of turbulent kinetic energy where a two-equation eddy viscosity model is employed would result in negative viscosity, which is not physically possible [43]. It was already mentioned that the UD scheme is bounded, however this is only achievable through a several degradation of accuracy.

The concept of flux-limiter was extensively used by van Leer. Methods that employ this idea are usually referred as "shock-capturing schemes", and resulted in Total Variation Diminishing (TVD) schemes. In a first approach these schemes were developed for supersonic flows, but were latter extended to general scalar transport [43]. Thus, the *van-Leer* discretization scheme is going to be employed for the advective terms present in the turbulence model equations.

4.3 Pressure Velocity Coupling

In a fluid mechanics problem, a total of five equations can be solved: the continuity equation, the energy equation and the set of momentum equations. A total of five unknowns are to be determined (p, T, u_x, u_y, u_z). Since the number of unknowns equals the number of equations, the system should be determined, thus simple to solve. However, there is not an equation that can directly solve the pressure present in that system. The continuity equation, rather than being an equation to be solved, is actually a restriction on each one of the three components of velocity. If the flow is compressible the continuity equation may be used as a transport equation for the density, and by using the equation of state $p = p(\rho, T)$, the pressure may be then obtained by the density [40]. However, if the flow is incompressible, the density is constant hence not linked to pressure. Furthermore, it is important to mention the non-linearity present in the advective terms of the momentum equations, which presents an increased difficulty in solving the system.

These problems can be resolved by adopting an iterative solution strategy in the pressure-velocity coupling linkage, such as the SIMPLE (Semi-Implicit Method for Pressure-Linked Equations) by Patankar and Spalding [56].

4.3.1 SIMPLE Algorithm

This algorithm is usually employed to produce steady state flow solutions in CFD. It can be summarized by Figure 4.5.

The first stage is to express the momentum equations in a general matrix form presented in Equation (4.5), where M is a matrix of coefficients that are calculated by discretizing the terms in the equation. This discretization can be made by employing the Finite Volume Method.

$$M\vec{u} = -\nabla \mathrm{p} \quad (4.5)$$

The momentum equations are now in a semi-discretized form. The system will have one equation per cell centroid. A key step is to separate the matrix M into diagonal and off-diagonal components. In Equation (4.6), the matrices A represents the diagonal compo-

nents and H the off-diagonal components.

$$A\vec{u} - H = -\nabla \mathrm{p} \quad (4.6)$$

This step is needed in order to easily invert the diagonal matrix and solve. By rearranging the momentum equation and substitute it into the continuity equation, a pressure correction equation is obtained, as in Equation (4.7).

$$\nabla \cdot (A^{-1}\nabla \mathrm{p}) = \nabla \cdot (A^{-1}H) \quad (4.7)$$

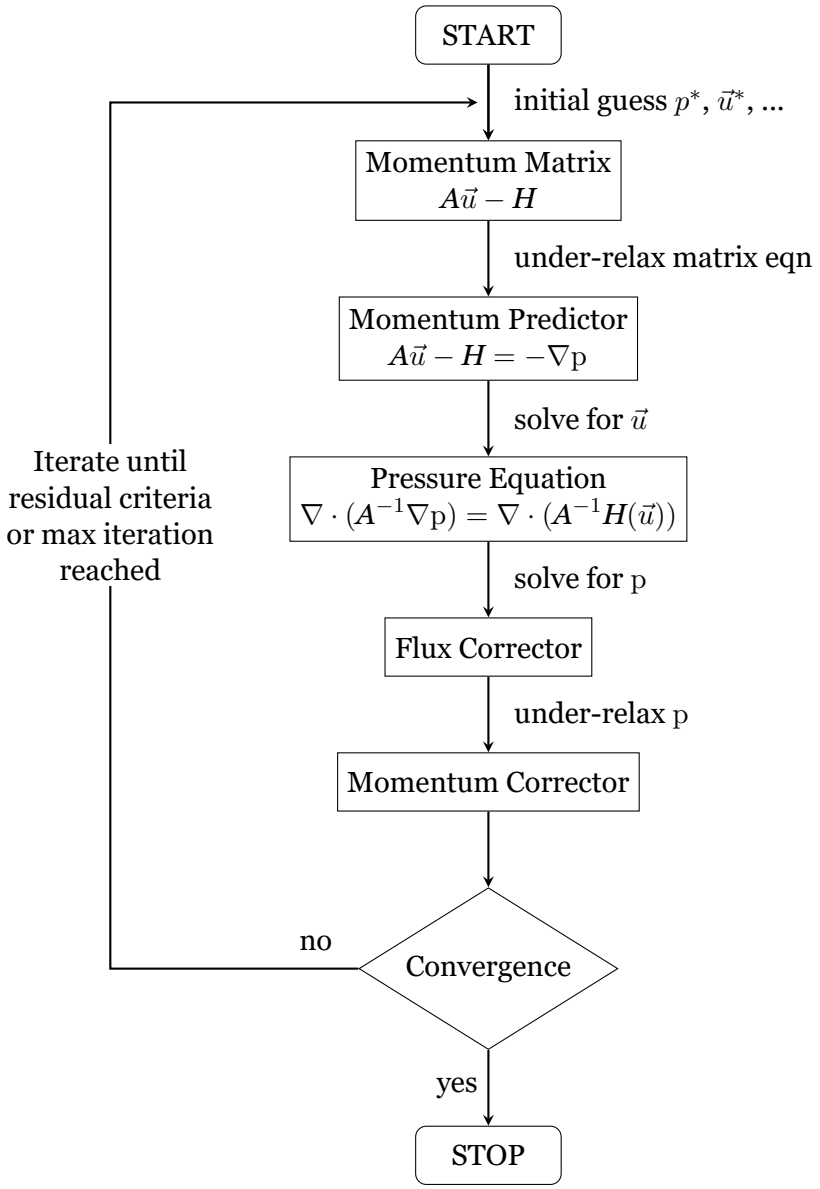

Figure 4.5: The SIMPLE algorithm [57].

Chapter 5

Implementation

OpenFOAM requires the choice of solvers for pressure, velocity and turbulent variables as well as several numerical schemes for the discretization of time domain, gradient, divergence and surface normal terms present in the governing equations, etc.. At the time of writing this thesis, experimental results for Omnidea, Lda's centrifugal pump were not available. Consequently, a search was conducted in order to find a study with both representative experimental results and geometrical data which allowed to replicate the pump geometry. The goal was to validate OpenFOAM's numerical setup with experimental data. Miner et al. [58], [59] and Flack et al. [60] performed studies where the same pump is utilized. Selim et al. [61] later performed numerical studies in order to evaluate the capability of modeling the experimental results with k-ε model. They display not only relevant experimental results but also dimensions which allow to accurately replicate the turbomachine. Results and information regarding this validation study are presented in Section 5.1.

5.1 Test Case - Validation

Miner et al. [58] performed laser velocimeter measurements in a medium specific speed centrifugal pump for design and off-design conditions. A total of five radial locations in four different windows were utilized to retrieve experimental velocity data with a total spatial uncertainty of $0.10\,\mathrm{m\,s^{-1}}$ for both radial and tangential velocities. Pressure probes were present 5 inlet pipe diameters upstream of the impeller, and around 3 inlet pipe diameters in the discharge to measure the pump characteristic curve. Its most relevant geometrical and working parameters are displayed in Table 5.1. Data regarding the environment and fluid conditions are not provided by the author, so the properties presented in Table 5.2 are adopted.

Table 5.1: Miner's centrifugal pump most relevant geometrical properties [58].

Property	Value	Unit
Inlet Tube Diameter	3.81×10^{-2}	[m]
Impeller Inlet Diameter	5.08×10^{-2}	[m]
Impeller Outlet Diameter	1.02×10^{-1}	[m]
Number of Blades	4	-
Pump Rotor Velocity	64.93	$[\mathrm{rad\,s^{-1}}]$
Nominal Flow Rate	6.30×10^{-3}	$[\mathrm{m^3\,s^{-1}}]$
Specific Speed	31.48	$[\mathrm{rad\,m^{3/2}\,s^{-3/2}}]$

Table 5.2: Environment conditions and relevant working fluid properties [58].

Property	Value	Unit
Fluid	Water	–
Environment Pressure	1.013×10^{5}	[Pa]
Environment Temperature	293.15	[K]
Fluid Density	998.2	$[\mathrm{kg\,m^{-3}}]$
Fluid Molecular Dynamic Viscosity	1.0016×10^{-3}	$[\mathrm{N\,s\,m^{-2}}]$

5.1.1 Sources of Error

There are some possible sources of error, alongside the error related to the discretization and the usage of RANS itself. The most probably sources of error are the following:

- Spatial discretization of the domain and usage of a Reynolds Averaged approach for the solving of the Navier-Stokes equations;
- No data regarding the environment pressure and temperature, which influences the density and molecular viscosity of the working fluid;
- Geometrical errors on the geometry. The lack of information in the original drawing presented by Miner et al. [58, 59] requires the need to resort to reverse engineering which usually comes with loss in accuracy and precision;
- Uncertainties associated with the location of pressure taps. Miner does not provide the exact location for the pressure tap located upstream of the impeller. The height of the fluid between the two probes is estimated to be around $19\,\mathrm{cm}$. The hydrostatic pressure represents 9.92% of the sum of static and hydrostatic pressures considering design operating conditions. It is then understandable that a slight variation in pressure taps placement presents a significant variation in pressure rise;
- The head versus flow rate points are not specified by Miner. A plot is presented, and the only point mentioned is the design point ($\Delta\mathrm{p} = 1.78\times10^{5}\,\mathrm{N\,m^{-2}}$, $\mathrm{Q} = 6.3\times10^{-3}\,\mathrm{m^3\,s^{-1}}$). The other points presented in this work are obtained resorting to reverse engineering.

Despite all the possible sources of error, and after an extensive research and the process of replicating several water centrifugal pumps, it was concluded that Miner's work was the one with more information regarding the geometrical characteristics of the pump, as well as relevant results.

5.1.2 Numerical Setup

This section is dedicated to explaining all the steps taken in this numerical study, with such detail that allows the replication of this study by whoever is reading it. The geometry and mesh are initially portrayed, boundary conditions are identified and finally results are presented. As the goal of this validation case is to obtain the pump characteristic curve, the mesh and boundary conditions portrayed below refer to a Multi Reference Frame steady state simulation.

5.1.2.1 Geometry and Meshing

A two dimensional projection of the geometry used is presented in Figure 5.1. Despite not being represented in this picture, there are two other geometries to have into consideration: a inlet which is part of the domain presented in Figure 5.1, and a inlet pipe which does not take part in that same domain. An independent simulation using the later one as domain is performed in order to obtain developed flow conditions for all the flow rates, which will be applied in the inlet of the pump. The length of the inlet was decided based on Selim et al. [61]. It was concluded that the effect of the pump in the inflow diminished with a length $\mathrm{L_{inlet}} = 3\mathrm{D_{inlet}}$. The pipe length was iterated until the velocity and turbulence intensity parameters did not change significantly. It was concluded that a length $\mathrm{L_{pipe}} = 40\mathrm{D_{inlet}}$ presented optimal results when considering the available computational resources. Morrison et al. [62] performed studies where similar results are achieved.

With the geometry defined, it is necessary to select the type of mesh to implement. The choice is just not about the type of element which typically provides the most accurate results. It is also necessary to take into consideration the available resources. Omnidea, Lda appealed for the usage of open source software whenever possible. Thus, the SALOME platform was used for mesh creation. It is a powerful tool which allows the creation of structured and unstructured tetrahedral and hexahedral meshes. Nevertheless, since the geometry in study is not a basic geometric shape, it was only possible to create a quad dominant unstructured mesh via two dimensional extrusion, as presented in Figure 5.2.

A benefit of unstructured grids already mentioned in Section 2.2 is the ease on implementing boundary layers cells. This last modification on the mesh was fulfilled after extracting the grid from SALOME. An OpenFOAM tool named *snappyHexMesh* was using since better results were achieved. Typically, turbulence models can resolve the flow down to the

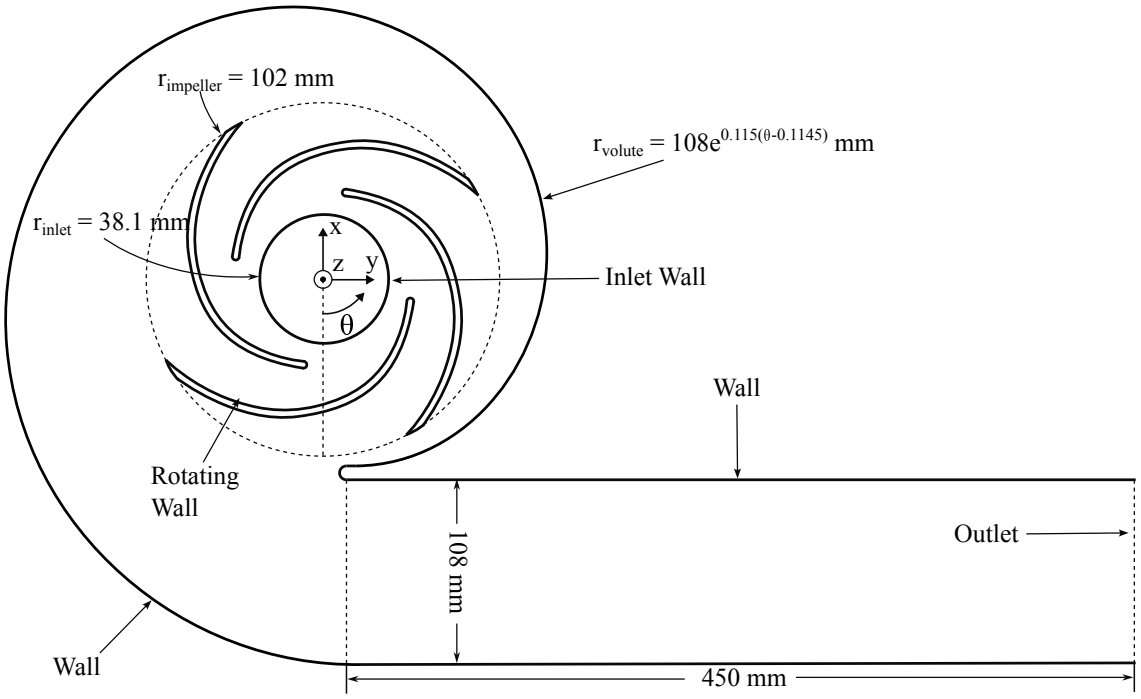

Figure 5.1: Domain representation and measurements (figure not up to scale).

viscous sublayer or make use of wall functions. As there is no need to evaluate heat transfer or forces, which is usually highly affected by the boundary layers mesh resolution, a high Reynolds approach was used for this problem. Furthermore, the available computational resources would set back this work by several weeks if the boundary layer would be completely solved. Thus, a y^+ between 30 and 200 was adopted.

It is then necessary to guarantee that the results obtained do not depend on the size of the finite volumes. A mesh independence study is performed based on the pressure rise. The initial iteration for the convergence was a number of elements was the one which allowed the elements to capture the curvature of the pump with acceptable detail (251928 volumes). The subsequent iterations were performed adding approximately the same number of elements elements to the previous one. Several authors [9, 25, 28] present a head versus number of elements or points plot as a mesh convergence criteria. However, the author of the present work considers the usage of a global parameter to be a mistake, since it captures only global behavior, and not local fluctuations. Consequently, in Figure 5.3, velocity profile curves for five different number of volumes at a specific radial location are displayed. Results are presented for the whole impeller, thus $0 \leq \theta \leq 360$. The values of θ where no velocity results are presented correspond to the blade location. Despite slight variations of velocity values, the three finer meshes provide similar results. Consequently, the mesh with $741\,672$ was selected. The grid quality parameters are of paramount importance when choosing discretization methods. These are presented in Table 5.3.

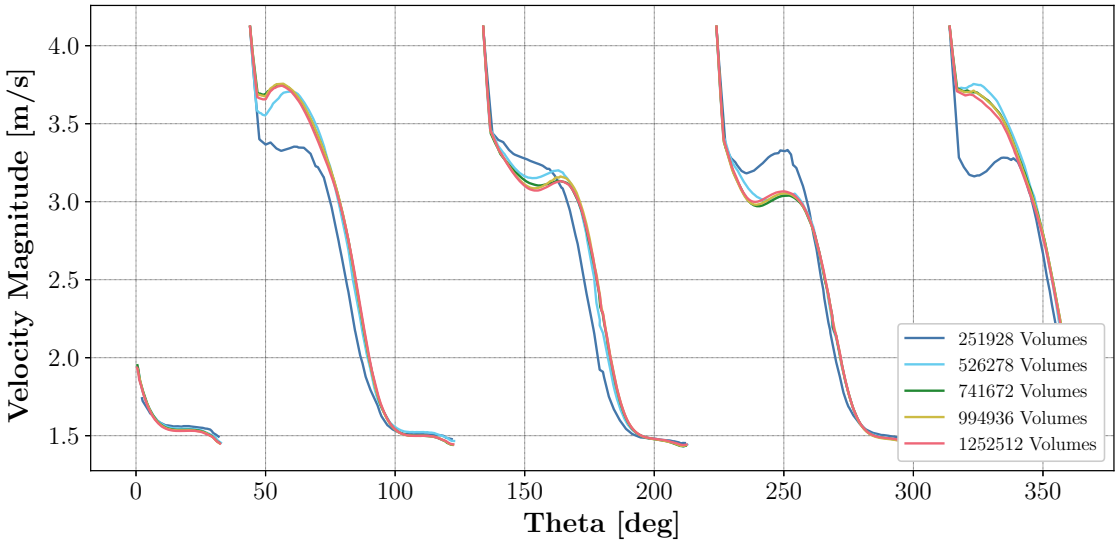

Figure 5.3: Impeller velocity magnitude profiles at a radial location $\mathrm{r} = 63.5$ mm, for $\mathrm{z} = 0$ mm for five different grids with $k - \varepsilon$ turbulence model.

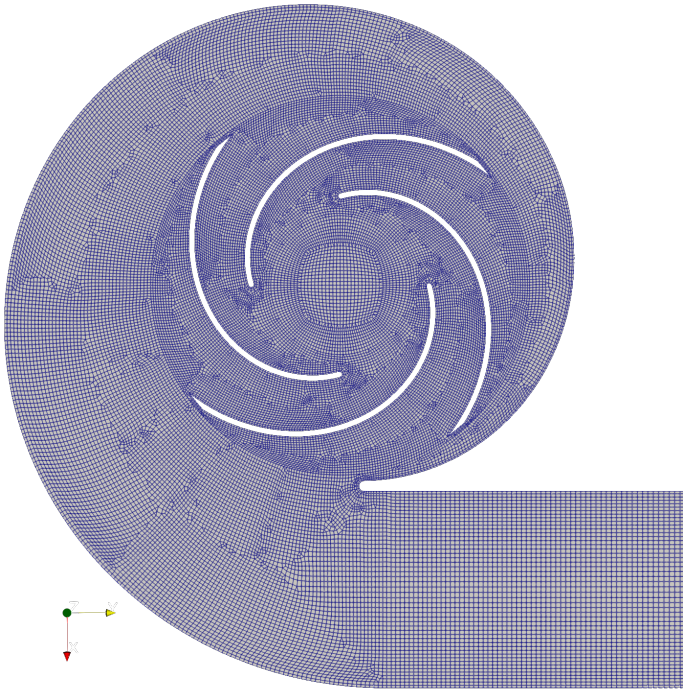

Figure 5.2: Detail of the mesh selected for the study.

Table 5.3: Grid quality parameters.

Maximum Aspect Ratio	13.8
Maximum Non-Orthogonality	54.0
Maximum Skewness	2.97
Number of Hexahedral Elements	723 936
Number of Tetrahedral Elements	17 736

5.1.2.2 Boundary Conditions

In this validation case there are two domains to be studied. The inlet pipe and the centrifugal pump itself. As mentioned already, the inlet conditions for the centrifugal pump are the outlet results from the inlet pipe simulation with one exception. The pump inlet velocity is set to be calculated based on the pressure calculated on the outlet of the pipe,

and a flow rate boundary condition is applied to the pump outlet. Consequently, the patch boundary conditions presented below refer to the inlet pipe.

OpenFOAM performs incompressible fluid calculation without using the fluid density when incompressible analysis are performed. Each component of the Navier-Stokes equations are divided by density and the pressure calculated by the software is actually the kinematic pressure. Thus, the boundary conditions related to pressure do not present a physical meaning. A static pressure of $0\ \mathrm{Pa}$ and $101\,325\ \mathrm{Pa}$ will produce the same head. Consequently, for the present simulation, choosing to use a pressure inlet or outlet boundary condition will present no result changes. In order to provide the results with a physical meaning, an inlet pressure boundary condition was chosen for this simulation where $\mathrm{p_{inlet}} = 101\,325\ \mathrm{Pa}$.

Since the static pressure was defined in the inlet, the velocity is to be specified in the outlet. This is done resorting to the *flowRateOutletVelocity* type in OpenFOAM, a velocity outlet boundary condition which corrects the extrapolated velocity to match a specified flow rate. Instead of assigning a single value for all the cell faces in the outlet patch, this boundary condition will adopt a velocity profile according to the distance from the walls, allowing for a smoother flow behavior. The actual volumetric flow rates will be modified depending on the point of the pump characteristic curve to be determined.

The turbulent kinetic energy and turbulent kinetic energy dissipation rate initial values are calculated based on Equation (5.1).

$$k = \frac{3}{2}(I|\vec{u}_{ref}|)^2 \quad , \quad \varepsilon = \frac{C_\mu^{0.75} k^{1.5}}{l_t} \tag{5.1}$$

where I is the turbulent intensity, $\vec{u}_{ref}$ is a reference velocity, $C_\mu = 0.09$ and l_t is the turbulent length scale, which depends on the geometry. Instead of defining a fixed value for each one of these variables, the *turbulenceIntensityKineticEnergyInlet* and *turbulenceMixingLengthDissipationRateInlet* boundary conditions present in OpenFOAM were adopted for k and ε, respectively. Just as the velocity boundary condition, instead of defining a fixed value for the patch cell faces, a value is calculated for each face depending on $\vec{u}_{ref}$ and k. Furthermore, it is necessary to define I and l_t. Russo and Basse [63] performed studies about turbulence intensity for low-speed smooth pipes was found. They summarized their experimental results for the turbulent intensity for incompressible pipe flow averaged over cross-sectional area in Equation (5.2), which will be considered for this work.

$$I = 0.140\mathrm{Re}^{-0.0790} \tag{5.2}$$

Regarding the turbulent length, Greenshields and Weller [57] present in their book Equa-

tion (5.3), which will be considered for this work.

$$l_t = 0.07D \quad (5.3)$$

With the patches boundary conditions defined, it is now important to mention the used wall boundary conditions. At all fixed walls, a no-slip condition is applied where both the normal and the tangential velocity components are set to zero. At moving walls, which is the case for the impeller blades, a rotating no-slip wall-velocity condition is applied where the moving reference frame is considered over the absolute one. This is done by using the *MRFnoSlip* condition in OpenFOAM.

5.1.3 Initialization and Convergence Criteria

A potential field approach is used in order to initialize the velocity field in the domain. For incompressible steady-state potential flows, the governing equation of the velocity potential satisfies the Laplace's equation, presented in Equation (5.4).

$$\nabla^2 \Phi = 0 \quad (5.4)$$

The velocity field can then be computed from the velocity potential as follows in Equation (5.5). This method is only employed for design conditions. The off-design initial values result from the results of the simulation with the closest flow rate from the one being performed.

$$\vec{u} = \nabla \Phi \quad , \quad \nabla \cdot \vec{u} = 0 \quad (5.5)$$

For the present work, the following criteria are used in order to evaluate convergence of results:

- Maximum Residual of 1×10^{-4} for the continuity, momentum, turbulent kinetic energy and turbulent kinetic energy dissipation rate equations;
- Maximum global imbalance of 1%;
- Maximum deviation of 0.1% in pressure probes results placed in strategical locations of the domain.

5.1.4 Results

The results obtained are presented in Figures 5.4 to 5.10. Firstly, the pump characteristic curve is displayed. Afterwards, despite being concluded by Dick et al. [1] and Mentzos et al. [23] that steady state simulations can not capture accurately velocity profiles inside the pump, plots comparing these numerical data are presented.

It is important to note that, for incompressible calculations, OpenFOAM v11 does not account for source terms. A modification to the source code would have to be performed, which would open the possibility to induce errors. This implies that no gravity is accounted on the simulations. Thus, an analytic correction was introduced where the hydrostatic pressure was calculated. The result came to $\mathrm{p_h} = 1859.9\ \mathrm{Pa}$. This value was added to the kinematic pressure on all the calculated design points and these are the results presented in Figure 5.4a. A power versus flow rate plot is also presented in Figure 5.4b.

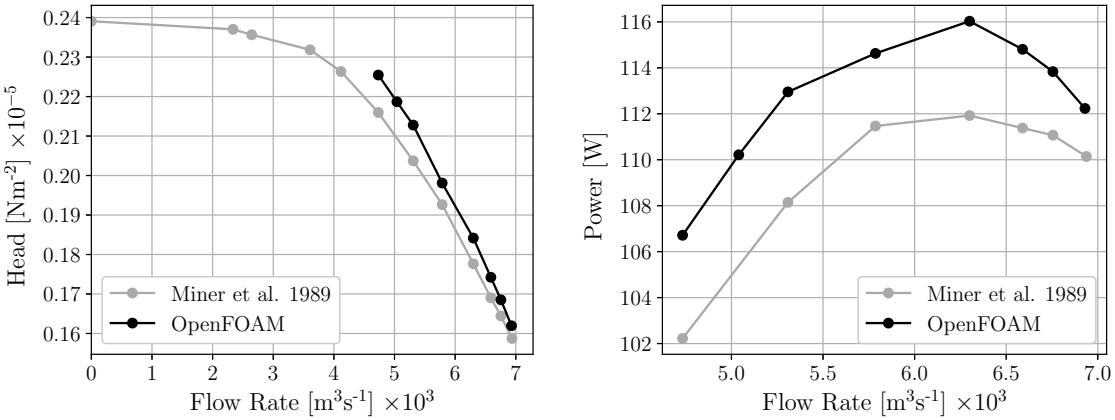

(a) (b)

Figure 5.4: Comparison of pump characteristic curve obtained from steady state analysis in OpenFOAM utilizing $k-\varepsilon$ turbulence model and experimental points from Miner et al. [58].

Regarding the pressure rise, a maximum and minimum errors of 4.30% and 2.02% are observed for the lowest and largest flow rates, $\mathrm{Q} = 0.751\mathrm{Q_0}$ and $\mathrm{Q} = 1.1\mathrm{Q_0}$, respectively. These results are in accordance to what is obtained by other authors. Wang et al. [9] records relative head discrepancies of 4% when the $k-\varepsilon$ model is used. Several authors [11, 12, 16, 21, 64] present minimal errors for design and slightly over-designed ($\mathrm{Q} < 1.1 < \mathrm{Q_0}$) conditions, where higher errors are recorded for the remaining flow rates. When it comes to the power plot a maximum and minumum errors of 4.37% and 1.90% are observed for $\mathrm{Q} = 0.8426\mathrm{Q_0}$ and for $\mathrm{Q} = 1.1\mathrm{Q_0}$, respectively. Both numerical and experimental analysis predict the best efficiency point to be at a flow rate equal to the design flow rate, with a deviation of 3.73%.

It is true that the pressure contours of a steady state simulation are not representative of what physically happens. Nevertheless, they can be used to compare results from similar

numerical calculations. Dick et al. [1] performed steady state and transient simulations based on the work produced by Miner et al. [58]. Results regarding gauge static pressure contours obtained by OpenFOAM calculations and Dick et al. are displayed in Figures 5.5 and 5.6, respectively. A reference pressure, $\mathrm{p_{ref}} = 101\,325\ \mathrm{Pa}$ utilized to calculate the gauge pressure, $\mathrm{p_{gauge}}$ in the present work is utilized. Dick et al. does not disclose the reference pressure value utilized.

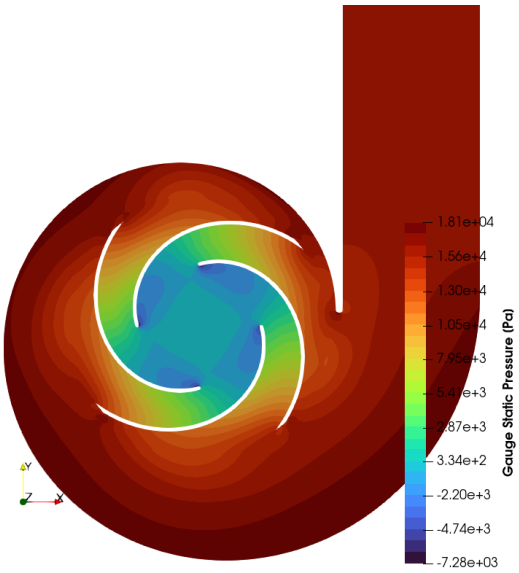

Figure 5.5: Calculated gauge pressure contour in mid plane at nominal flow rate $\mathrm{Q} = 6.3{\times}10^{-3}\ \mathrm{m^3\,s^{-1}}$ modeled with $k-\varepsilon$ turbulence model. Reference pressure, $\mathrm{p_{ref}} = 101\,325\ \mathrm{Pa}$.

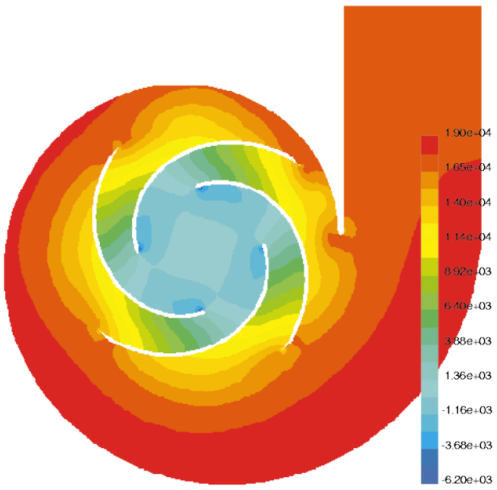

Figure 5.6: Gauge pressure contour in mid plane at nominal flow rate $\mathrm{Q} = 6.3{\times}10^{-3}\ \mathrm{m^3\,s^{-1}}$ modeled with Realizable $k-\varepsilon$ turbulence model. Adapted from [1].

After analyzing results retrieved by OpenFOAM and Dick et al. [1], it is clear that a similitude between pressure distribution is present. An increase in velocity in the trailing edge of the blades, a decrease in pressure in the outlet section of the pump, and similar locations of the stagnation point present in the volute tongue and blades leading edges are observed in both studies. When comparing maximum and minimum values of both plots a difference in values is present. The author believes that it is due to the pressure reference used to calculate the gauge pressure. This is because, when a pressure difference calculation is performed, the values of $\Delta \mathrm{p_{gauge,1}} = 25\,380\ \mathrm{Pa}$ and $\Delta \mathrm{p_{gauge,2}} = 25\,200$ are obtained for the OpenFOAM calculations and Dick et al. [1] works, respectively, which represents a relative error of 0.71%.

Lastly, a comparison between velocity profiles is performed. Numerical steady state results obtained from OpenFOAM, transient numerical results obtained from Selim et al. [61] and experimental data points from Miner et al. [59] are presented in Figures 5.8 to 5.10 The total uncertainty for both radial and tangential components of the experimental data is $0.10\ \mathrm{m\,s^{-1}}$. This will make it possible to understand wether it is viable to perform steady state analysis in order to replicate velocity profiles in a centrifugal pump. Never-

theless, before presenting the results themselves, it should be explained how they were retrieved on all the three studies.

The goal is to capture how the velocity vectors behave over an average of the pump blade passages, in two points. In order to define a point in a cylindrical reference frame, a radial and an angular position must be defined. Consequently, three radial positions ($r = 63.5$ mm, $r = 88.9$ mm, $r = 100.3$ mm) were chosen. In each of the radial positions, two angular locations were also defined ($\theta = 0\ °$, $\theta = 180\ °$), defining a total of six points, as presented in Figure 5.7. However, in a numerical steady state simulation where time is not considered and the grid is stationary, blade-averaged results at defined points in space would simply translate into a constant plot of velocity over blade passage. In order to surpass this, the radial segments which intersected the points at the defined angular positions were chosen, as seen in Figure 5.7. The segments representing $\theta = 180°$ and $\theta = 0°$ are in blue and orange, respectively. The PS and SS acronyms represent the pressure side and suction side of the blade, respectively.

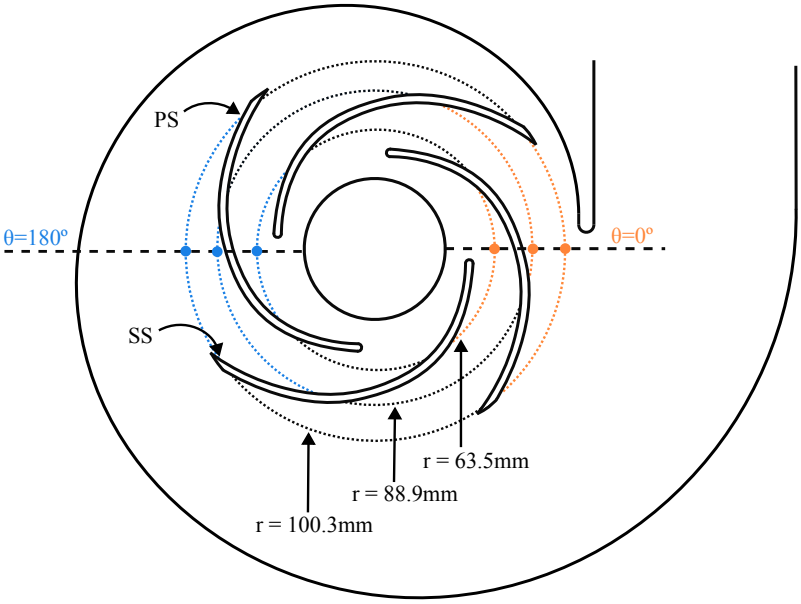

Figure 5.7: Representation of velocity profile measurement locations for Selim et al. [61] and Miner et al. [59] portrayed by blue and orange dots, and the radial blade segments passage utilized to present results from OpenFOAM numerical steady state simulations, presented by blue and orange dotted lines. Figure not up to scale

The velocity profiles are presented in Figures 5.8 to 5.10. Results from OpenFOAM calculations are displayed as an average of ten planes parallel to the YX plane, for ten z locations. On the other hand, results from Selim et al. [61] are only presented for the mid plane, which the author of this work does not consider to be completely accurate, since the laser velocimeter measurement method used by Miner et al. [58, 59] will capture particles on all z locations.

When analyzing Figure 5.8, an almost perfect match in experimental and OpenFOAM

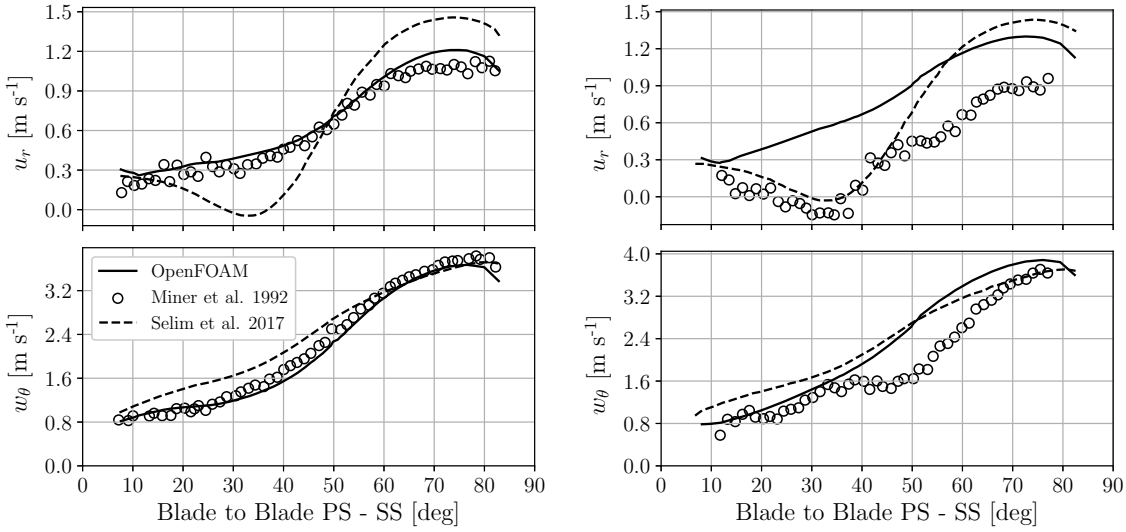

(a) $\theta = 180$ °

(b) $\theta = 0$ °

Figure 5.8: Radial and relative tangential velocity at $\mathrm{r} = 63.5\ \mathrm{mm}$.

for $\theta = 180°$ results can be seen. Steady state results are closer to experimental ones than the transient ones obtained by Selim et al. [61]. Nonetheless, this does not mean that the steady state approach is neither more accurate nor precise. As will be seen in following radial positions, and even for this same radial position but on a different angular position, the transient calculations will always present a more similar curve behavior to the experimental. This discrepancy presented in Figure 5.8a is believed to be cause by the fact that the transient results are being displayed for the mid plane, and not as an average, thus not taking into account the third dimensional effect on the flow. This third dimensional effect is stronger for smaller radius, since it is closer to the inlet. As the radius increases, the third velocity component, u_z, starts becoming relatively smaller. In Figure 5.8b, the steady state numerical scheme fails to capture both radial and tangential flow behavior. Between 20° to 40°, a negative radial velocity is registered by Miner et al., which means that a inlet recirculation is occurring. This could be interpreted as a failure of the $k - \varepsilon$ model to replicate adverse pressure gradient zones. Nevertheless, Selim et al. also utilized the $k - \varepsilon$ model and it is capturing the recirculation region. This is seen as a failure of the steady state approach to capture an unsteady phenomena. There is also a presence of a constant tangential velocity region at $\theta = 0°$, which is neither captured by the steady state nor the transient approaches, for the $k - \varepsilon$ turbulence model. With this being said, Selim et al. [61] presents results for the Realizable $k - \varepsilon$ model, which captures this phenomena, meaning a failure of the $k - \varepsilon$ model to capture this.

Looking at Figure 5.9, a decrease in velocity profiles similarity is observed for $\theta = 180°$, and an increase for $\theta = 0°$. When comparing the results from Figure 5.9 with Figure 5.8, two conclusions can be drawn. There is not only a decrease in blade loading but also in the radial component of velocity, u_r. Blade loading is the difference in the pressure acting on the pressure and suction surfaces of a blade [6]. For $r = 63.5\ \mathrm{mm}$, a positive blade loading

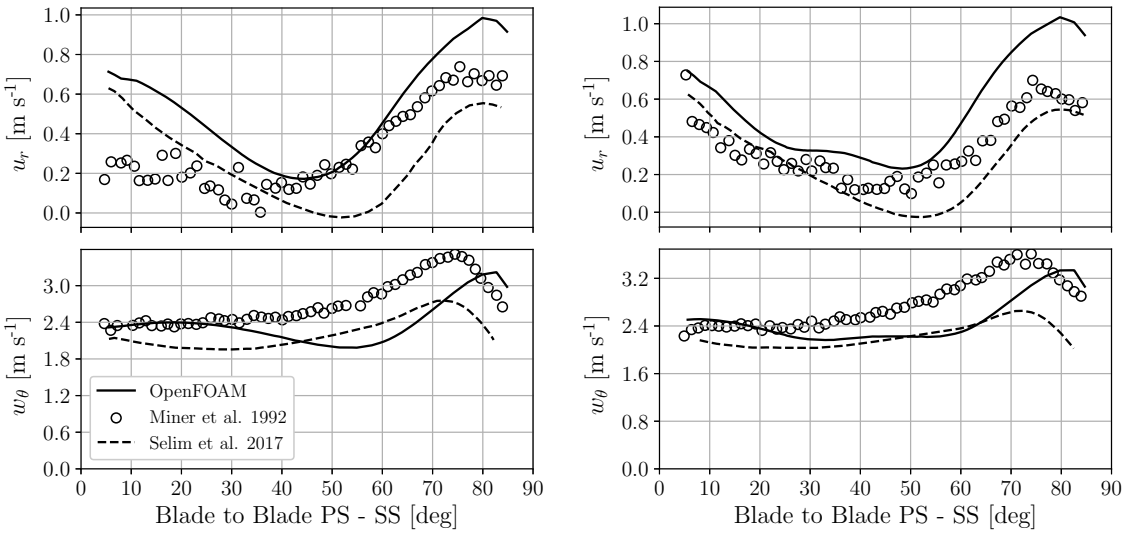

(a) $\theta = 180$ °

(b) $\theta = 0$ °

Figure 5.9: Radial and relative tangential velocity at $\mathrm{r} = 88.9$ mm.

is observed, which means that relative velocity increases from the pressure surface to the suction surface. The same happens for $r = 88.9$ mm, however with lower intensity and with a decrease in radial velocity for between pressure and suction sides. If comparing the numerical calculations between themselves, an over prediction of u_r is observed for the steady analysis, and an under prediction for u_r is observed on the transient analysis. This happens at around half the blade passage from the pressure side for $\theta = 180°$ and on the whole extent of the blade passage for $\theta = 0°$

Finally, let us consider the most outer radius, $r = 100.3$ mm, which is close to the impeller exit. When analyzing Figure 5.10, it is easily perceived that this radial position is where most differences between steady state numerical calculations and experimental data are present. The steep decrease in radial velocity u_r observed both in transient and experimental data is not present in the steady state analysis. Furthermore, at around $65°$ of the blade passage, an almost zero radial velocity is observer, which translate into a start of recirculation that is not present in the real case. This behavior occurs for both angular positions. Moreover, when paying close attention to $\theta = 0°$, an unusual change in u_r and w_ω can be observed for a blade passage position of $45°$: an increase in both components of velocity. This blade passage position is aligned with the volute tongue, which is believed to be the cause for this occurrence. When comparing w_ω in both angular positions, an increase in velocity immediately after the pressure side is perceived, which is the opposite of what happens with transient and experimental data. Nevertheless, when comparing the global behavior of the velocity profiles for this radius, a negative blade loading is observed, contrary on what happened to the first two radial positions. This phenomena is called jet-wake phenomenon, which is common to appear in radial blades.

After analyzing Figures 5.8 to 5.10 it can be concluded that velocity profiles tend to be more

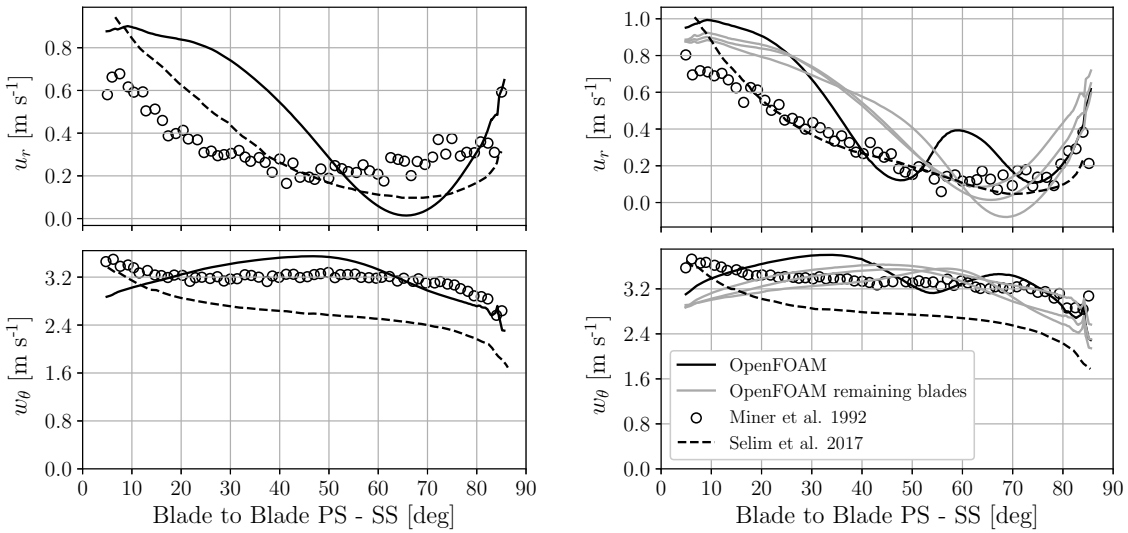

(a) $\theta = 180\ ^\circ$ (b) $\theta = 0\ ^\circ$

Figure 5.10: Radial and relative tangential velocity at $\mathrm{r} = 100.3\ \mathrm{mm}$.

similar when comparing results at a smaller radial position. When close to the impeller outlet, numerical steady state analysis is not able to predict a correct flow behavior. In the overall, if velocity distribution or secondary flow phenomena is of importance, a numerical transient analysis must be performed.

5.2 Omnidea's Centrifugal Pump

In this section, the geometry and characteristics of Omnidea's centrifugal pump will be presented. While it was initially intended to analyze the pump's performance, the simulations were ultimately discarded due to a lack of computational resources and insufficient time to implement necessary cavitation and multiphase flow models. The absence of these models prevented an accurate representation of regions where the pressure drops below the fluid's vapor pressure, which is critical in cryogenic applications. Firstly, the pump characteristics are displayed. As the design is confidential, data regarding the geometry can not be fully disclosed. These are displayed in Table 5.4 while the information of the working fluid and pressure conditions is presented in Table 5.5.

Table 5.4: Omnidea's centrifugal pump most relevant geometrical properties.

Property	Value	Unit
Number of Impeller Blades	8	-
Number of Inducer Blades	2	-
Pump Rotor Velocity	4115.5	$[\mathrm{rad\,s^{-1}}]$
Nominal Flow Rate	5.37×10^{-3}	$[\mathrm{m^3\,s^{-1}}]$
Specific Speed	20.34	$[\mathrm{rad\,m^{3/2}\,s^{-3/2}}]$

Table 5.5: Environment conditions and relevant working fluid properties for Omnidea's centrifugal Pump.

Property	Value	Unit
Fluid	LOx	–
Inlet Pressure	2.10×10^{5}	[Pa]
Inlet Fluid Temperature	92	[K]
Fluid Density	1132.3	$[\mathrm{kg\,m^{-3}}]$
Fluid Molecular Dynamic Viscosity	1.8584×10^{-3}	$[\mathrm{N\,s\,m^{-2}}]$

5.2.0.1 Pump Schematic

Omnidea's centrifugal pump, like most rocket engine pumps, incorporates an inducer to enhance its performance in cryogenic conditions. The inducer, located upstream of the impeller, serves to pre-pressurize the liquid oxygen (LOx) before it enters the main impeller. This design helps to mitigate cavitation—a critical issue in cryogenic environments where low temperatures cause the fluid to approach its vapor pressure. By reducing cavitation risks, the inducer ensures a more stable flow and higher overall efficiency, which is essential for maintaining reliable pump operation in rocket

Contrary to the first test case presented in Section 5.1, this turbomachine can not be described with a two dimensional projection due to the presence of an inducer and the double curvature of the impeller blades. The schematic of Omnidea's centrifugal pump, shown in Figure 5.11, identifies key components and their respective boundary conditions. The pump consists of several distinct regions: the inlet (marked in blue) and the outlet (green), both of which correspond to the static walls of the pump (gray). The impeller blades (pink) and inducer (red) are rotating components, driving the fluid flow through the pump. The hub (cyan) is also a rotating part, contributing to the overall motion of the fluid. The inlet pipe is oriented horizontally, while the outlet pipe extends vertically. This schematic provides an essential overview of the pump's operational regions, which are critical for setting up the boundary conditions in the numerical simulation.

Similarly to the first test case, an independent pipe study was carried out in order to input a developed profile for the inlet of the pump domain. The pipe length is also forty times the pump's inlet diameter. Regarding the pump's inlet tube, a inlet legth $\mathrm{L_{inlet}} = 6\mathrm{D_{inlet}}$ was applied.

Due to the higher complexity of geometry, the meshing process was not done resorting to SALOME, but to the *snappyHexMesh* tool instead. This is a tool implemented with OpenFOAM which uses a hexahedral background mesh as a base for the final mesh. The

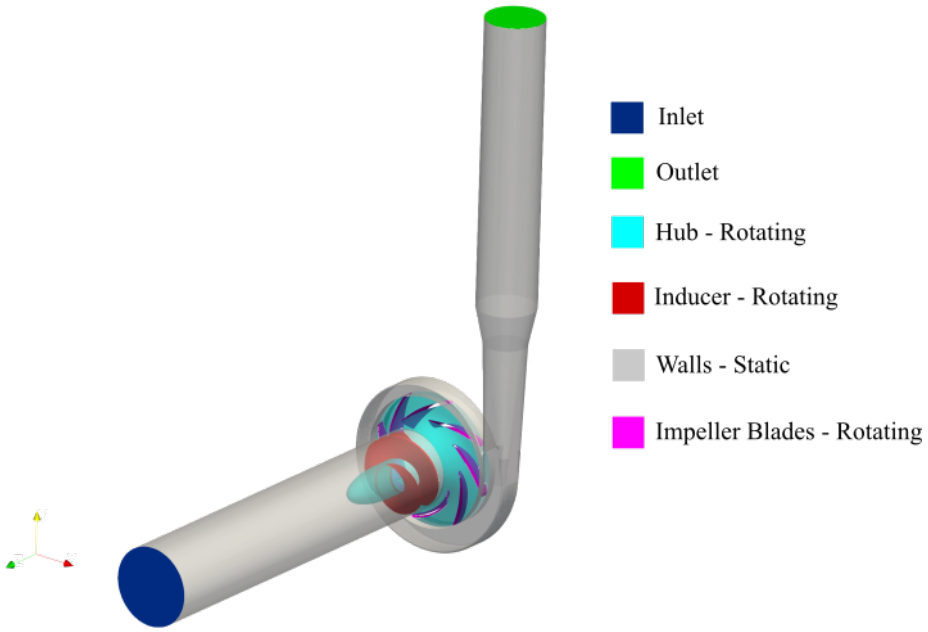

Figure 5.11: Omnidea's centrifugal pump domain boundaries.

background mesh can possess several formats. The ones considered for this case were cartesian cubic mesh or a cylindrical mesh. Since it was not possible to achieve a mesh that correctly followed the solid walls of the domain with a cylindrical approach, the cartesian cubic approach was used instead. The reason for the usage of this tool was that SALOME could not build a hexahedral mesh, and the number of tetrahedral elements was around three to four times the hexahedral elements. In Figures 5.12 and 5.13 are presented front and side views of the final mesh, respectively.

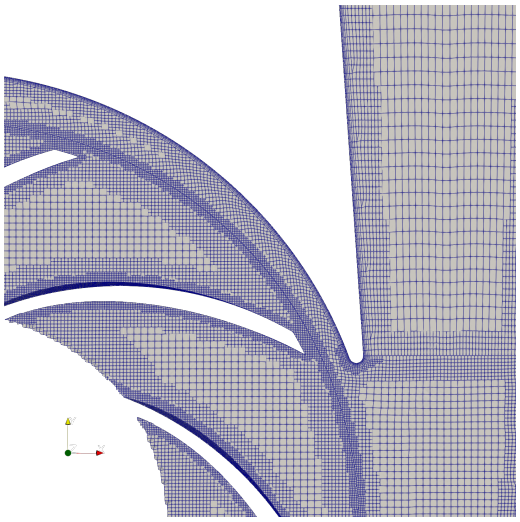

Figure 5.12: Front view of the grid for Omnidea's centrifugal pump

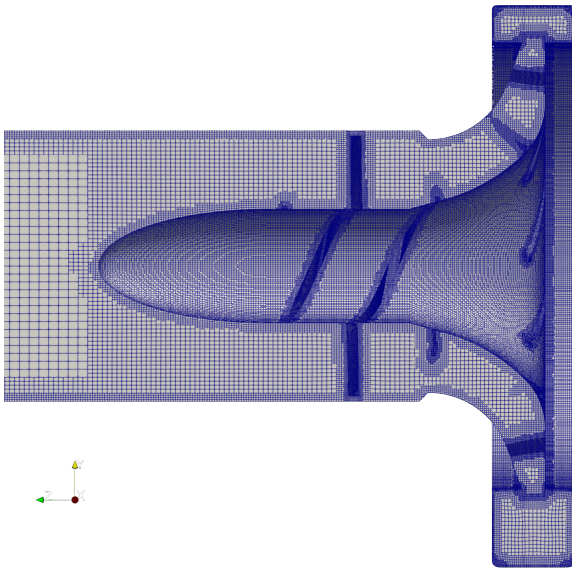

Figure 5.13: Side view of the grid for Omnidea's centrifugal pump

In conclusion, although the analysis of Omnidea's centrifugal pump was ultimately not

Table 5.6: Omnidea's centrifugal pump grid quality parameters.

Maximum Aspect Ratio	Maximum Non-Orthogonality	Maximum Skewness	Number of Hexahedral Elements	Number of Polyhedral Elements	Number of Prism Elements
18.8	69.3	3.84	5 697 631	603 672	185 646

performed due to the limitations mentioned earlier—namely, the lack of computational resources and the time required to implement critical cavitation and multiphase flow models—this section provides a comprehensive overview of the pump's design and characteristics. The geometry, boundary conditions, and mesh configuration have been detailed to offer insight into the complexity of the model. While the numerical analysis was not completed, the provided data and figures illustrate the steps that would have been taken had the analysis proceeded, offering a clear understanding of how the pump would have been studied in greater depth.

Chapter 6

Conclusions and Future Work

This study focused on the numerical analysis of a centrifugal pump using the OpenFOAM software, with an emphasis on validating the model against experimental data and understanding the performance of the pump under various operating conditions. The key findings from this research are as follows:

- **Model Validation and Performance**: The numerical simulations performed using the standard $k - \varepsilon$ turbulence model demonstrated good agreement with experimental results for global parameters like total head and power, with maximum errors of 4.30% and 4.37%, respectively. The prediction of the best efficiency point had a deviation of 3.73% in flow rate compared to the experimental data by Miner et al.
- **Numerical Challenges**: The study revealed limitations in simulating conditions where cavitation might occur, as the current model did not incorporate a two-phase flow model or a detailed cavitation model. This limitation prevented accurate simulation in areas where the pressure falls below the fluid's vapor pressure, highlighting the need for more advanced modeling techniques for such scenarios.
- **Model Reliability and Applicability**: Despite these limitations, the numerical approach proved to be a valuable tool for predicting the overall performance of centrifugal pumps in conditions where the flow remains relatively simple and cavitation-free. The developed model's reliability for practical engineering applications was confirmed through the validation against experimental data.
- **Impeller and Flow Analysis**: The velocity profiles in relation to blade passage showed less satisfactory results, indicating the need for more detailed mesh refinement and potentially more advanced turbulence modeling to capture the complex flow dynamics accurately. This suggests areas for improvement in future studies to enhance the model's predictive capability.

Building upon the findings of this research, several directions for future work have been identified to address the limitations and enhance the capabilities of the numerical model:

- **Incorporation of Cavitation Models**: Future studies should integrate cavitation models to simulate conditions where the pressure drops below the vapor pressure of the fluid. This will enable the analysis of cavitation effects on pump performance and help in designing pumps that are more resistant to cavitation damage.

- **Advanced Turbulence Modeling**: Implementing more sophisticated turbulence models, such as the Large Eddy Simulation (LES) or Detached Eddy Simulation (DES), could provide better insights into the complex flow behaviors around the impeller and volute, particularly for transient and unsteady flow conditions.
- **Two-Phase Flow Simulations**: Extending the model to include two-phase flow simulations will allow for the examination of pumps handling fluids with varying phases, which is critical for accurately predicting performance in applications involving multiphase flows.
- **Mesh Refinement and Adaptive Gridding**: Further refinement of the computational mesh, particularly near the blades and in regions of high velocity gradients, along with the use of adaptive meshing techniques, could improve the accuracy of velocity profiles and reduce numerical errors.
- **Experimental Validation**: Additional experimental validation with a wider range of operating conditions and different pump designs will help to further verify and refine the numerical model. This will enhance its robustness and applicability to various engineering scenarios.
- **Broader Application Scope**: Expanding the application of the model to other types of turbomachinery, such as axial flow pumps and compressors, could provide valuable insights and contribute to the development of more generalized and versatile modeling approaches.

At the outset of this master's dissertation, ambitious objectives were outlined. The project aimed to develop a cavitation model that could simulate the thermodynamic effects in cryogenic fluids within a pump-scale CFD framework. Additionally, the implementation of a multi-phase model was part of the initial scope. However, as evidenced by the content of this document, these initial goals were not fully realized. Over the 13 months dedicated to this thesis, the majority of time was allocated to three primary activities: identifying scientific papers with adequate geometrical data and relevant results to use as validation cases, conducting meshing and re-meshing of the computational domain, and resolving numerical errors that stemmed from improper meshing of the geometry.

It is now clear that these factors can stretch timelines significantly. In hindsight, the timeline could have been cut, but wrapping up the project earlier by accepting the dysfunction of the enhanced cavitation model yet enticed by meeting the original vision, the project was kept on for longer.

Despite the challenges, extending the timeline allowed for a deeper understanding of the complexities involved and provided valuable insights into the intricacies of meshing and error resolution in computational fluid dynamics. This prolonged effort, although initially frustrating, resulted in a more thorough comprehension of the limitations and potential improvements in CFD modeling. The extended duration also highlighted the importance

of meticulous pre-processing and validation, reinforcing the necessity for robust meshing tools and practices. Such insights are invaluable for future projects and contribute to the overall advancement of the field.

In conclusion, this research has laid a solid foundation for the numerical analysis of centrifugal pumps and has identified critical areas for further investigation and improvement. By addressing the outlined future work, the numerical models can be refined and expanded to provide more accurate and reliable tools for the design and analysis of advanced pumping systems in various industrial applications.

Bibliography

[1] E. Dick, J. Vierendeels, S. Serbruyns, and J. Vande Voorde, "Performance prediction of centrifugal pumps with cfd-tools," *TASK QUARTERLY*, vol. 5, pp. 579–594, Jan 2001. xv, 14, 15, 46, 47

[2] G. P. Sutton and O. Biblarz, *Rocket Propulsion Elements*, 9th ed. Wiley, 2017. 1, 2, 10

[3] S. L. Dixon and C. A. Hall, *Fluid Mechanics and Thermodynamics of Turbomachinery*, 7th ed. Elsevier, 2014. 5, 6, 19

[4] I. J. Karassik, *Pump Handbook*, 4th ed. McGraw-Hill, 2008. 1, 6

[5] G. Gakhun, "АТЛАС КОНСТРУКЦИЙ ЖРД ЧАСТЬ ii," Московский ордена Ленина авиационный институт имени Серго Орджоникидзе, Moscow, Tech. Rep., 1973.

[6] J. F. Gülich, *Centrifugal Pumps*. Berlin ; New York: Springer, 2008. 1, 7, 8, 9, 13, 19, 49

[7] W. E. Campbell and J. Farquhar, "Centrifugal pumps for rocket engines," NASA, Tech. Rep., 1974. 10

[8] S. Shah, S. Jain, R. Patel, and V. Lakhera, "CFD for centrifugal pumps: A review of the state-of-the-art," *Procedia Engineering*, vol. 51, pp. 715–720, 2013. [Online]. Available: http://dx.doi.org/10.1016/j.proeng.2013.01.102 11, 15

[9] Y. Wang, H. Liu, S. Yuan, M. Tan, and M. Shu, "Applicability of turbulence models on characteristics prediction of centrifugal pumps," in *ASME-JSME-KSME 2011 Joint Fluids Engineering Conference*, vol. 1, no. https://doi.org/10.1115/AJK2011-03022, Hamamatsu, Shizuoka, Japan, Jul 2011, pp. 85–91. [Online]. Available: https://doi.org/10.1108/hff-07-2014-0205 12, 14, 17, 30, 42, 46

[10] Y. Wang and W. J. Wang, "Applicability of eddy viscosity turbulence models in low specific speed centrifugal pump," in *IOP Conference Series: Earth and Environmental Science*, vol. 15, Nov 2012, p. 062013. [Online]. Available: https://doi.org/10.1088/1755-1315/15/6/062013 12, 14, 17, 30

[11] A. Nocente, T. Arslan, and T. K. Nielsen, "Numerical prediction of a multistage centrifugal pump performance with stationary and moving mesh," in *ASME 2015 Power Conferecne*, San Diego, California, USA, Jun 2015. [Online]. Available: https://doi.org/10.1115/POWER2015-49119 12, 14, 46

[12] S. Huang, Y. Wei, C. Guo, and W. Kang, "Numerical simulation and performance prediction of centrifugal pump's full flow field based on openfoam," *Processes*,

vol. 7, no. 605, 2019. [Online]. Available: https://doi.org/10.3390/pr7090605 12, 14, 17, 30, 31, 46

[13] X. Wu, J. Feng, H. Liu, J. Ding, and H. Chen, "Performance prediction of single-channel centrifugal pump with steady and unsteady calculation and working condition adaptability for turbulnce model," in *Transactions of the Chinese Society of Agricultural Engineering*, vol. 33, Jan 2017, pp. 85–91. [Online]. Available: https://doi.org/10.1108/hff-07-2014-0205 12

[14] X. Li, Y. Ji, H. Cui, and S. Xue, "Comparative study on turbulence models of high-speed centrifugal pump with low specific speed," in *IOP Conf. Ser.: Mater. Sci. Eng.*, vol. 141, no. 740, Jan 2020. [Online]. Available: http: doi.org/10.1088/1757-899X/740/1/012038 12

[15] J. Wang, Y. Wang, H. Liu, H. Huang, and L. Jiang, "An improved turbulence model for predicting unsteady cavitating flows in centrifugal pump," *International Journal of Numerical Methods for Heat & Fluid Flow*, vol. 25, no. 5, pp. 1198–1213, Jun 2015. [Online]. Available: http://doi.org/10.1108/HFF-07-2014-0205 12, 17

[16] K. Cheah, T. Lee, S. Winoto, and Z. Zhao, "Numerical flow simulation in a centrifugal pump at design and off-design conditions," *International Journal of Rotating Machinery*, vol. 2007, Apr 2007. [Online]. Available: https://doi.org/10.1155/2007/83641 12, 46

[17] S.-S. Hong, D.-J. Kim, J.-S. Kim, C.-H. Choi, and J. Kim, "Study on inducer and impeller of a centrifugal pump for a rocket engine turbopump," *Proceedings of the Institution of Mechanical Engineers, Part C: Journal of Mechanical Engineering Science*, vol. 227, no. 2, pp. 311–319, May 2012. [Online]. Available: http:doi.org/10.1177/0954406212449939 13

[18] B. Yang, B. Li, H. Chen, Z. Liu, and K. Xu, "Numerical investigation of the clocking effect between inducer and impeller on pressure pulsations in a liquid rocket engine oxygen turbopump," *Journal of Fluids Engineering*, vol. 141, no. 7, Jul 2019. [Online]. Available: http:doi.org/10.1115/1.4042160 13

[19] E. Blanco-Marigorta, J. Fernandez-Francos, and J. Gonzalez-Perez, "Numerical flow simulation in a centrifugal pump with impeller–volute interaction," in *Proceedings of ASME FEDSM'00*, Boston, Massachusetts, June 2000. 13

[20] R. Spence and J. Amaral-Teixeira, "Investigation into pressure pulsations in a centrifugal pump using numerical methods supported by industrial tests," *Computers & Fluids*, vol. 37, pp. 690–704, Jul 2008. [Online]. Available: https://doi.org/10.1016/j.compfluid.2007.10.001 13, 14, 17

[21] J. Gonzalez, C. Santolaria, F. Castro, and M. T. Parra, "Numerical model for the unsteady flow behaviour inside a double suction pump," in *Proceedings of*

ASME FEDSM'03, vol. 1, Honolulu, Hawaii, USA, Jan 2003. [Online]. Available: https://doi.org/10.1115/FEDSM2003-45396 13, 14, 46

[22] J. Gonzalez, J. Fernandez, E. Blanco, and C. Santolaria, "Numerical simulation of the dynamic effects due to impeller-volute interaction in a centrifugal pump," *Journal of Fluids Engineering*, vol. 124, no. 2, pp. 348–355, Jun 2002. [Online]. Available: http://doi.org/10.1115/1.1457452 13, 14, 15, 17, 30

[23] M. Mentzos, A. Filios, D. Margaris, and D. Papanikas, "A numerical simulation of the impeller-volute interaction in a centrifugal pump," in *1st International Conference "From Scientific Computing to Computational Engineering"*, Athens, Greece, Sep 2004. [Online]. Available: https://doi.org/10.1088/1755-1315/15/6/062013 13, 46

[24] M. Shojaeefard, M. Tahani, M. Ehghaghi, M. Fallahian, and M. Beglari, "Numerical study of the effects of some geometric characteristics of a centrifugal pump impeller that pumps a viscous fluid," *Computers & Fluids*, vol. 60, pp. 61–70, May 2012. [Online]. Available: http://dx.doi.org/10.1016/j.compfluid.2012.02.028 14, 17, 30

[25] H. Alemi, S. A. Nourbakhsh, M. Raisee, and A. F. Najafi, "Effects of volute curvature on performance of a low specific-speed centrifugal pump at design and off-design conditions," *Journal of Turbomachinery*, vol. 137, no. 4, p. 041009, Apr 2015. [Online]. Available: https://doi.org/10.1115/1.4028766 14, 17, 26, 30, 42

[26] Y. Bai, D. Appiah, and Y. Tao, "Computational turbulent flow characteristics in a centrifugal pump," *AIP Advances*, vol. 12, no. 7, p. 075025, Jul 2022. [Online]. Available: http://doi.org/10.1063/5.0100915 14, 17

[27] G. Mousmoulis, I. Kassanos, G. Aggidis, and I. Anagnostopoulos, "Numerical simulation of the performance of a centrifugal pump with a semi-open impeller under normal and cavitating conditions," *Applied Mathematical Modelling*, vol. 89, pp. 1814–1834, Jan 2021. [Online]. Available: http://doi.org/10.1016/j.apm.2020.08.074 14, 17, 30

[28] Y. Fu, J. Yuan, S. Yuan, G. Pace, L. d'Agostino, P. Huang, and X. Li, "Numerical and experimental analysis of flow phenomena in a centrifugal pump operating under low flow rates," *Journal of Fluids Engineering*, vol. 137, p. 011102, Jan 2015. [Online]. Available: https://doi.org/10.1115/1.4027142 14, 17, 30, 42

[29] R. Spence and J. Amaral-Teixeira, "A cfd parametric study of geometrical variations on the pressure pulsations and performance characteristics of a centrifugal pump," *Computers & Fluids*, vol. 37, pp. 1243–1257, Dec 2008. [Online]. Available: https://doi.org/10.1016/j.compfluid.2008.11.013 14

[30] Z. Li, P. Wu, D. Wu, and L. Wang, "Experimental and numerical study of transient flow in a centrifugal pump during startup," *Journal of Mechanical*

Science and Technology, vol. 25, no. 3, pp. 749–757, 2011. [Online]. Available: http://doi.org/10.1007/s12206-011-0107-7 14, 17, 30

[31] X. Zheng, W. Wang, P. Zhang, Y. Pu, and Y. Zhao, "Internal flow characteristics of centrifugal pumps under different startup combination schemes," *Water*, vol. 16, no. 1087, 04 2024. [Online]. Available: https://doi.org/10.3390/w16081087 15

[32] L. A. R. Golding and W. A. Smith, *Centrifugal Pumps - Now and the Future*, 1995, pp. 142–151. [Online]. Available: https://doi.org/10.1007/978-3-642-79340-0_14 15

[33] I. Gibson, D. Rosen, and B. Stucker, *Additive Manufacturing Technologies*, 2nd ed. Springer, 2015. 15

[34] G. H. Schnerr and J. Sauer, "Physical and numerical modeling of unsteady cavitation dynamics," in *4th International Conference on Multiphase Flow*, New Orleans, USA, May 2001. 17

[35] P. J. Zwart, A. G. Gerber, and T. Belamri, "A two-phase flow model for predicting cavitation dynamics," in *5th International Conference on Multiphase Flow*, no. 152, Yokohama, Japan, May 2004. 17

[36] M. Auvinen, J. Ala-Juusela, N. Pedersen, and T. Siikonen, "Time-accurate turbomachinery simulations with open-source cfd; flow analysis of a single-channel pump with openfoam," in *V European Conference on Computational Fluid Dynamics*, Jun 2010. 17

[37] H. Schlichting and K. Gersten, *Boundary-Layer Theory*, 9th ed. Berlin, Heidelberg: Springer Berlin Heidelberg, 2017. 19, 20

[38] F. M. White, *Fluid Mechanics*, 8th ed. New Delhi, India: McGraw-Hill Education, 2017. 20

[39] S. B. Pope, *Turbulent Flows*. Cambridge University Press, 2000. 21

[40] H. K. Versteeg and W. Malalasekera, *An introduction to computational fluid dynamics: the finite volume method*, 2nd ed. Harlow, England ; New York: Pearson Education Ltd, 2007. 11, 21, 23, 35

[41] C. Hirsch, *Numerical computation of internal and external flows: fundamentals of computational fluid dynamics*, 2nd ed. Elsevier/Butterworth-Heinemann, 2007. 22, 24, 29, 30

[42] M. Buchmayr, "Development of fully implicit block coupled solvers for incompressible turbulent flows," PhD thesis, Graz University of Technology, Graz, Austria, January 2014. 23, 29, 30

[43] H. Jasak, "Error analysis and estimation for the finite volume method with applications to fluid flows," PhD thesis, Imperial College, London, England, June 1996. 25, 29, 30, 32, 33, 34, 35

[44] J. Boussinesq, "Théorie de l'écoulement tourbillant," *Mémoires présentés par divers savants à l'Académie des Sciences*, vol. 23, p. 46, 1987. 25

[45] E. Dick and S. Kubacki, "Transition models for turbomachinery boundary layer flows: A review," *International Journal of Turbomachinery, Propulsion and Power*, vol. 2, no. 2, Apr 2017. [Online]. Available: http://doi.org/10.3390/ijtpp2020004 26

[46] B. Launder and S. D.B., "The numerical computation of turbulent flows," *Computer Methods in Applied Mechanics and Engineering*, vol. 3, no. 2, pp. 269–289, 1974. [Online]. Available: https://doi.org/10.1016/0045-7825(74)90029-2 11, 26, 27

[47] F. Menter, "Two-equation eddy-viscosity turbulence models for engineering applications," *AIAA journal*, vol. 32, no. 8, pp. 1598–1605, Aug 1994. [Online]. Available: https://doi.org/10.2514/3.12149 11

[48] F. Menter, M. Kuntz, and R. Langtry, "Ten years of industrial experience with the sst turbulence model," *Heat and Mass Transfer*, vol. 4, pp. 625–632, Jan 2003.

[49] C. Direct. (2022) Openfoam non-conformal coupling. [Online]. Available: https://cfd.direct/openfoam/free-software/non-conformal-coupling/ 31

[50] C. J. Greenshields, *OpenFOAM User Guide version 11*, 1st ed. OpemFOAM Foundation Ltd., 2023. 31, 33

[51] F. Moukalled, L. Mangani, and M. Darwish, *The Finite Volume Method in Computational Fluid Dynamics*, 1st ed. Switzerland: Springer, 2016. 32

[52] J. H. Ferziger and M. Peric, *Computational Methods for Fluid Dynamics*, 3rd ed. Springer, 2003. 34

[53] M. Perić, "A finite volume method for the prediction of three-dimensional fluid flow in complex ducts," PhD thesis, Imperial College, London, Aug 1985. 34

[54] W. Shyy, "A study of finite difference approximations to steady-state, convection-dominated flow problems," *Journal of Computational Physics*, vol. 57, pp. 415–438, 1985. [Online]. Available: https://doi.org/10.1016/0021-9991(85)90188-3 34

[55] J. E. Fromm, "A method for reducing dispersion in convective difference schemes," *Journal of Computational Physics*, vol. 3, pp. 176–189, 1968. [Online]. Available: https://doi.org/10.1016/0021-9991(68)90015-6 34

[56] S. V. Patankar and D. B. Spalding, "A calculation procedure for heat, mass and momentum transfer in three-dimensional parabolic flows," *Heat and Mass*

Transfer, vol. 15, pp. 1787–1806, 1972. [Online]. Available: https://doi.org/10.1016/B978-0-08-030937-8.50013-1 35

[57] C. Greenshields and H. Weller, *Notes on Computational Fluid Dynamics: General Principles*. Reading, UK: CFD Direct Ltd, 2022. 37, 44

[58] S. M. Miner, R. J. Beaudoin, and R. D. Flack, "Laser velocimeter measurements in a centrifugal flow pump," *Journal of Turbomachinery*, vol. 111, no. 3, pp. 205–212, Jul 1989. [Online]. Available: https://doi.org/10.1115/1.3262257 39, 40, 46, 47, 48

[59] S. M. Miner, R. D. Flack, and P. E. Allaire, "Two-dimensional flow analysis of a laboratory centrifugal pump," *Journal of Turbomachinery*, vol. 114, no. 2, pp. 333–339, Apr 1992. [Online]. Available: https://doi.org/10.1115/1.2929147 39, 40, 47, 48

[60] R. D. Flack, S. M. Miner, and R. J. Beaudoin, "Turbulence measurements in a centrifugal pump with a synchronously orbiting impeller," *Journal of Turbomachinery*, vol. 114, no. 2, pp. 350–358, Apr 1992. [Online]. Available: https://doi.org/10.1115/1.2929149 39

[61] S. M. Selim, M. A. Hosien, S. M. El-Behery, and M. Elsherbiny, "The influence of turbulence modeling technique on centrifugal pump simulation," in *17th International Conference on Aerospace Sciences and Aviation Technology*, Cairo, Egypt, Apr 2017. [Online]. Available: https://doi.org/10.21608/asat.2017.22755 39, 41, 47, 48, 49

[62] G. L. Morrison, K. R. Hall, J. C. Holste, L. Ihfe, C. Gaharan, and R. E. J. Deotte, "Flow development downstream of a standard tube bundle and three different porous plate flow conditioners," *Flow Measurement and Instrumentation*, vol. 8, no. 2, pp. 61–76, Jun 1997. [Online]. Available: https://doi.org/10.1016/S0955-5986(97)00021-6 41

[63] F. Russo and N. T. Basse, "Scaling of turbulence intensity for low-speed flow in smooth pipes," *Flow Measurement and Instrumentation*, vol. 52, pp. 101–114, 12 2016. [Online]. Available: https://doi.org/10.1016/j.flowmeasinst.2016.09.012 44

[64] ——, "Numerical simulation research on radial force of centrifugal pump with guide vanes," *Shock and Vibration*, vol. 2021, 01 2021. [Online]. Available: https://doi.org/10.1155/2021/6638123 46